OULU 2014
C 484

ACTA UNIVERSITATIS OULUENSIS


*Jani Mäklin*

# ELECTRICAL AND THERMAL APPLICATIONS OF CARBON NANOTUBE FILMS

*UNIVERSITY OF OULU GRADUATE SCHOOL;*
*UNIVERSITY OF OULU,*
*FACULTY OF INFORMATION TECHNOLOGY AND ELECTRICAL ENGINEERING,*
*DEPARTMENT OF ELECTRICAL ENGINEERING*

ACTA UNIVERSITATIS OULUENSIS
C Technica 484

*JANI MÄKLIN*

# ELECTRICAL AND THERMAL APPLICATIONS OF CARBON NANOTUBE FILMS

Academic dissertation to be presented with the assent of the Doctoral Training Committee of Technology and Natural Sciences of the University of Oulu for public defence in OP-sali (Auditorium L10), Linnanmaa, on 9 April 2014, at 12 noon

UNIVERSITY OF OULU, OULU 2014

Copyright © 2014
Acta Univ. Oul. C 484, 2014

Supervised by
Professor Krisztián Kordás

Reviewed by
Professor Laszlo Nanai
Doctor Asta Kärkkäinen

ISBN 978-952-62-0385-0 (Paperback)
ISBN 978-952-62-0386-7 (PDF)

ISSN 0355-3213 (Printed)
ISSN 1796-2226 (Online)

Cover Design
Raimo Ahonen

JUVENES PRINT
TAMPERE 2014

**Mäklin, Jani, Electrical and thermal applications of carbon nanotube films.**
University of Oulu Graduate School; University of Oulu, Faculty of Information Technology and Electrical Engineering, Department of Electrical Engineering
*Acta Univ. Oul. C 484, 2014*
University of Oulu, P.O. Box 8000, FI-90014 University of Oulu, Finland

***Abstract***

Carbon nanotubes (CNTs) have fascinating mechanical, electrical and thermal properties, all of which significantly depend on structural properties such as nanotube length, number of walls, lattice defect densities, impurities and surface functional groups. A number of different applications of carbon nanotubes have been demonstrated during the past two decades including electrical interconnects, transistors, heating and cooling devices, sensors and various actuators. However, further studies on the structure-dependent properties and innovative handling techniques of these materials are needed in order to explore the limitations of use and to be able fully to exploit the advantageous properties of such one-dimensional $sp^2$ hybridized carbon nanomaterials.

In this thesis, random networks of single-wall and multi-walled carbon nanotubes (SWCNTs and MWCNTs, respectively) and aligned films of multi-walled carbon nanotubes are studied in the context of three main application fields: gas sensing, electrical interconnects/electrodes and thermal cooling elements. Analyses of associated material properties and some feasible integration techniques are discussed.

Single-wall and multi-walled carbon nanotube films cast from aqueous dispersions are shown to be selective nitric oxide sensing components in Taguchi-type sensor devices, in which films based on SWCNTs outperformed those made of MWCNTs. The thickness dependent electrical conduction mechanism of inkjet-printed SWCNT films is also discussed. Robust aligned MWCNT films are demonstrated as soft electrical contact brushes in DC motors and in other moving electrical contacts. The thermal properties of freestanding aligned MWCNT forests are analyzed and shown to be potential alternatives to copper or aluminium in the thermal management of electrical components.

*Keywords:* carbon nanotubes, chip cooling, electrical contacts, electrical transport, gas sensors, solder transfer, thermal management

**Mäklin, Jani, Hiilinanoputkista koostuvien kalvojen sähköiset ja termiset sovellukset.**
Oulun yliopiston tutkijakoulu; Oulun yliopisto, Tieto- ja sähkötekniikan tiedekunta, Sähkötekniikan osasto
*Acta Univ. Oul. C 484, 2014*
Oulun yliopisto, PL 8000, 90014 Oulun yliopisto

### *Tiivistelmä*

Hiilinanoputkien kiehtovat mekaaniset, sähköiset ja lämmönjohto-ominaisuudet ovat kiinnostaneet tutkijoita suuresti viimeisten kahden vuosikymmenen ajan. Monia erilaisia applikaatioita on demonstroitu tänä aikana: mukaan lukien sähköiset kontaktit, transistori-rakenteet, lämmitys- ja jäähdytyslaitteet, anturirakenteet sekä erilaiset aktuaattori-rakenteet.

Tämän väitöskirjan päätavoitteena on tutkia hiilinanoputkien toiminnollisuutta ja käytännöllisyyttä erilaisissa sovelluskohteissa. Tässä työssä käytettävät hiilinanoputkirakenteet ovat joko satunnaisjärjestyksessä olevia nanoputkista koostuvia verkostorakenteita tai yhdensuuntaisia, makroskooppisia hiilinanoputkikalvoja. Nanoputkia tutkitaan kolmessa erityyppisessä sovelluskohteessa: kaasuanturisovelluksessa, sähköisissä kontaktirakenteissa sekä jäähdytyselementteinä. Työssä analysoidaan hiilinanoputkirakenteiden ominaisuuksia eri sovelluskohteissa sekä esitetään joitain käyttökelpoisia tekniikoita hiilinanoputkien integroimiseen olemassa oleviin tekniikoihin.

Hiilinanoputkien osoitetaan olevan käyttökelpoisia aktiivisia materiaaleja typpioksidille resistiivisessä kaasuanturirakenteessa. Tulosten perusteella yksiseinämäiset hiilinanoputket ovat moniseinämäisiä herkempiä ja parempia kyseisessä sovelluksessa. Lisäksi tutkitaan ja analysoidaan mustesuihku-tulostettujen yksiseinämäisten hiilinanoputkifilmien sähköisten ominaisuuksien riippuvuutta filmin paksuudesta. Vantterien yhdensuuntaisten moniseinämäisten hiilinanoputkirakenteiden osoitetaan toimivan erinomaisesti pehmeinä sähköisinä kontaktielementteinä liikkuvissa sähköisissä kontakteissa. Vapaasti seisovien yhdensuuntaisten, moniseinämäisten hiilinanoputkirakenteiden lämmönjohto-ominaisuuksien tutkiminen ja analysointi osoittaa, että kyseisiä rakenteita voidaan käyttää tehokkaina jäähdytyselementteinä ja mahdollisesti korvaavana vaihtoehtona alumiinille ja kuparille sähköisten komponenttien lämmönhallinta sovelluksissa.

*Asiasanat:* hiilinanoputket, juotosliitos, kaasuanturit, komponenttien jäähdytys, lämmönhallinta, sähköiset kontaktit, sähkönjohtavuus

*”The best research results are always found at home.”*
*Peter Heszler (1958-2009)*

# Acknowledgements

This work was done at the Microelectronics and Materials Physics Laboratories of the University of Oulu during the years 2008-2013. The work was mainly carried out in the frameworks of SANES (Integrated Self-Adjusting Nano-Electronic Sensors) and Thema-CNT (Thermal management with carbon nanotube architectures) projects funded by European Union (EU-STREP).

I wish to thank my supervisor and friend Professor Krisztián Kordás who gave me the opportunity and resources to do this research. His ambition and broad knowledge on materials science have inspired me during the years we have worked together. He is not only a true scientist but also a nice guy to get along with. I also gratefully thank Professor Heli Jantunen for her helpful guidance in the post graduate studies. I especially thank Dr. Antti Uusimäki for lively discussions and off-topic activities during the years at the University. I wish to thank the whole personnel of the Microelectronics and Materials Physics Laboratories for making the work enjoyable. I am also grateful to Pekka Moilanen for technical assistance and guidance. I also acknowledge all the other guys working for the Center of Microscopy and Nanotechnology in University of Oulu. I wish also thank the whole research group in which I worked for many years. I especially thank Tero Mustonen, Geza Tóth, Niina Halonen, Olli Pitkänen, Jarmo Kukkola, Anne-Riikka Leino and all the other personnel which have helped me during the years.

This work has been financially supported by Riitta ja Jorma J. Takanen foundation, Tauno Tönning foundation and Ulla Tuominen foundation.

I wish to thank my parents and other relatives for their support during my studies. Most of all, I show my utmost respect and gratitude to my beautiful and lovely wife Heljä. Without your love and support this work would have never been done. I dedicate this work to my family, especially to my three adorable children: Malviina, Maksimus and Minerva. You are the best!

Oulu, December 2013 Jani Mäklin

# List of symbols and abbreviations

The list of units, symbols and the list of abbreviations are in alphabetical order.

| | |
|---|---|
| % | per cent |
| ° | degree |
| °C | degree Celsius |
| A | ampere |
| A | average area of the cross section |
| $A^*$ | Richardson's constant |
| $\bar{a}_1$, $\bar{a}_2$ | unit vectors of graphene lattice |
| $c_h$ | lattice vector of graphene |
| e, q | elementary charge |
| eV | electron volt |
| F | farad |
| g | gram |
| H | fenry |
| h | Planck's constant |
| Hz | hertz |
| J | current density |
| J | joule |
| k | Boltzmann's constant |
| K | kelvin |
| kg | kilogram |
| L | litre |
| m | metre |
| m | number of Schottky junctions |
| $m^*$ | effective mass of charge carriers |
| $m_e$ | mass of an electron |
| min | minute |
| mL | mililitre |
| N | newton |
| p | pressure |
| Pa | pascal |
| ppm | parts per million |
| $R_0$ | initial resistance |
| s | second |

| | |
|---|---|
| T | temperature |
| Torr | unit of pressure (= 1mm Hg) |
| V | volt |
| W | watt |
| $\Delta R$ | change in resistance |
| $\theta$ | chiral angle of graphene |
| $\Phi_b$ | Schottky barrier height |
| $\Omega$ | ohm |

| | |
|---|---|
| 1/f noise | noise in which signal is inversely proportional to the frequency |
| AC | alternating current |
| $Al_2O_3$ | aluminium (III) oxide or alumina |
| Aspect ratio | width/height ratio of a shape |
| CCVD | catalytic chemical vapour deposition |
| CFD | computational fluid dynamics |
| $CH_4$ | methane |
| CNT | carbon nanotube |
| CO | carbon monoxide |
| DC | direct current |
| DUT | device under test |
| DWCNT | double-walled carbon nanotube |
| EFTEM | energy-filtered transmission electron microscopy |
| EMF | electromotive force |
| EtOH | ethanol |
| FES | fluctuation enhanced sensing |
| FESEM | field-emission scanning electron microscopy |
| FET | field-effect-transistor |
| HF | hydrofluoric acid |
| $I_D/I_G$ | ratio of D– and G–band intensities in Raman spectra |
| $I_{S-D}$ | source-drain current |
| I–V | current-voltage |
| LabVIEW | Laboratory Virtual Instrumentation Engineering Workbench |
| LDA | linear discriminant analysis |
| MATLAB | numerical computing environment developed by MathWorks |
| m-CNT | metallic carbon nanotube |
| MWCNT | multi-walled carbon nanotube |
| $N_2$ | nitrogen |

| | |
|---|---|
| NO | nitric oxide |
| $NO_x$ | nitric oxides |
| $NO_2$ | nitrogen dioxide |
| $N_2O_4$ | dinitrogen tetroxide |
| PCA | principal component analysis |
| PECVD | plasma enhanced chemical vapour deposition |
| PSD | power spectral density |
| RBM | radial breathing mode |
| RIE | reactive ion etch |
| rpm | revolutions per minute |
| SCCM | standard cubic centimetres per minute |
| s-CNT | semiconducting carbon nanotube |
| SMD | surface-mount device |
| SWCNT | single-wall carbon nanotube |
| TEM | transmission electron microscopy |
| TIM | thermal interface material |
| TMS | temperature modulated sensing |
| $U_G$ | gate voltage |
| USB | universal serial bus |
| wt% | per cent in weight |

# List of original papers

This thesis consists of an overview and the following five publications:

I Mäklin J, Mustonen T, Kordás K, Saukko S, Tóth G & Vähäkangas J (2007) Nitric oxide gas sensors with functionalized carbon nanotubes. Physica Status Solidi B 244(11): 4298–4302.

II Mustonen T, Mäklin J, Kordás K, Halonen N, Tóth G, Saukko S, Vähäkangas J, Jantunen H, Kar S, Ajayan PM, Vajtai R, Helistö P, Seppä H & Moilanen H (2008) Controlled Ohmic and nonlinear electrical transport in inkjet-printed single-wall carbon nanotube films. Physical Review B 77(12): 125430 1–7.

III Tóth G, Mäklin J, Halonen N, Palosaari J, Juuti J, Jantunen H, Kordás K, Sawyer WG, Vajtai R & Ajayan PM (2009) Carbon-Nanotube-Based Electrical Brush Contacts. Advanced Materials 21(1): 1–5.

IV Mäklin J, Halonen N, Tóth G, Sápi A, Kukovecz Á, Kónya Z, Jantunen H, Mikkola J-P & Kordás K (2011) Thermal diffusivity of aligned multi-walled carbon nanotubes measured by the flash method. Physica Status Solidi B 248(11): 2508–2511.

V Mäklin J, Halonen N, Pitkänen O, Tóth G & Kordás K (2014) Solder transfer of carbon nanotube microfin coolers to ceramic chips. Applied Thermal Engineering 65(1–2): 539–543.

Paper I introduces the use of carbon nanotubes as gas sensing material on alumina templates with gold electrodes. Stable solutions of both single-wall carbon nanotube (SWCNT) and multi-walled carbon nanotube (MWCNT) inks were prepared for the deposition of CNT films used as sensing material for nitric oxide (NO). The performance of both types of sensor was tested and compared. It was found that SWCNTs outperformed their MWCNT counterparts due to the tunable Fermi-level in the semiconducting nanotubes.

In paper II the electrical transport properties of inkjet deposited SWCNT networks - deposited on aluminum oxide and silicon chips - were evaluated. CNT films of good surface coverage showed linear (ohmic) behaviour, while low density networks displayed nonlinear (Schottky type) current–voltage characteristics. The results indicated that printed CNTs can be used as both interconnect and semiconducting channels e.g. in thin film transistor applications.

Paper III shows the feasibility of aligned multiwalled carbon nanotube brushes as a new high-performance electrical brush contact material. The MWCNT electrical contact brushes were used both as rotating axles and sliding contacts in electrical motors. In the rotating axle configuration the CNTs were directly grown on quartz rods while in the sliding contact configuration the CNT blocks were mounted on flexible brass cantilevers. Both AC and DC electrical

properties were investigated as well as the reliability of such contacts. Here, the structural integrity, compressibility and good electrical conductivity of aligned macroscopic nanotube films were exploited. The results showed that CNT films are appropriate alternatives to conventional sliding/rotating electrical contacts. The soft but durable MWCNT brushes showed stable, low-noise operation for extended periods of operation, thus opening new possibilities to integrate CNTs into existing technologies. Paper III was noticed in the media world-wide, including in ScienceDaily.

In paper IV the thermal properties of thick (> 1 mm), freestanding MWCNT forests are studied. The nanotubes were grown by the catalytic chemical vapour deposition (CCVD) method and the thermal diffusivity and conductivity of freestanding MWCNT forests were measured by a flash method. The results showed that MWCNT films can outperform ordinary thermal interface materials and may be alternative counterparts to aluminum (Al) and copper (Cu) components in thermal management applications. Thermal treatment of nanotube forests was found to decrease the thermal diffusivity and conductivity of the samples.

Paper V shows the usage of MWCNT forests as efficient cooling elements in ceramic chip cooling applications. The CCVD grown MWCNTs were transferred to ceramic ($Al_2O_3$) chips using a soldering process. The CNT forests were metal-enhanced by a thin coating of Cr/Au (15 nm/ 450 nm) and subsequently soldered onto ceramic test chips using conventional SAC–paste (Sn–Ag–Cu). The efficiency of such a cooling structure was examined and compared to a Cu-based reference cooler. The results showed similar or even slightly improved cooling efficiency when using a CNT-based cooler compared to its Cu-based counterpart. Paper V shows that the integration of CNTs into existing technologies is achievable.

The CNT synthesis, planning of experiments, optical characterization (excluding TEM), analyses and data processing were mostly the contribution of the author. In Paper II the contribution of the author was the planning, performing and analyzing of the electrical measurements. In Paper III the experiments were done in association with Dr.Tech. Geza Tóth. Si-chips used in experiments were provided by M.Sc. Niina Halonen. The manuscripts were written by the author with the kind help of co-authors. The measurement programs used in the electrical measurements in Papers I, II and III were written by the author using the LabVIEW environment.

# Contents

# 1 Introduction

## 1.1 Carbon nanotubes

It is generally agreed that carbon nanotubes (CNTs) were discovered in 1991 by Iijima, even though the first discoveries of nanosized tubular carbon structures were reported much earlier (Radushkevich & Lukyanovich 1952, Millward & Jefferson 1976, Oberlin et al. 1978). Those early findings were not available for the whole scientific community, thus Iijima's (Iijima 1991) and Dresselhaus' (Dresselhaus *et al*. 1992) ground breaking reports were necessary to initiate the subsequent considerable research in the field (Figure 1).

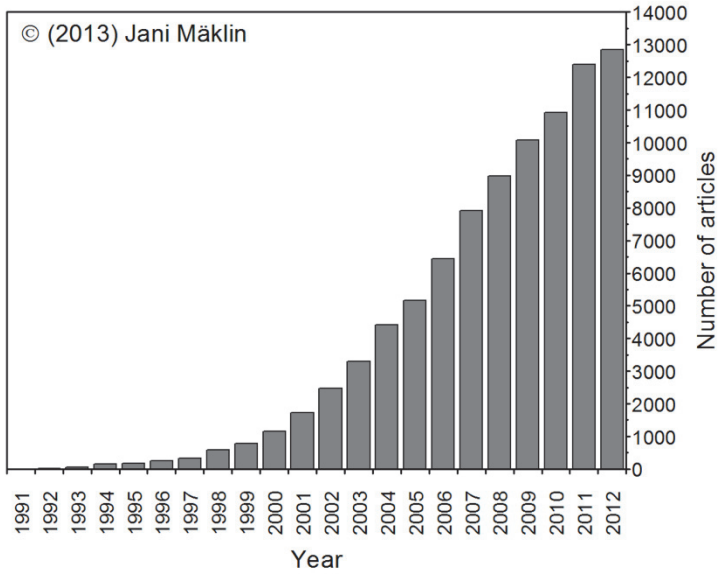


**Fig. 1. Number of publications found in Thomson Reuters Web of Knowledge using keyword "carbon nanotube". Search was performed on 18.06.2013.**

CNTs are composed of carbon atoms linked in hexagonal shapes, with each carbon covalently bonded to three other carbon atoms. They can be described as $sp^2$ hybridized graphene sheets (a single atomic layer of graphite) rolled up into a cylinder, forming a tubular structure. The tube ends are normally capped with hemi-spherical structure but they can also be open. CNTs can be characterized

into different categories depending on how many graphitic layers they have: single-wall (SWCNT), double-walled (DWCNT) and multi-walled (MWCNT). Carbon nanotubes have diameters ranging from 1 nm (SWCNT) up to tens of nanometres (MWCNT). The length of a nanotube can be from nanometres up to several centimetres. They exhibit the most extreme diversity in structure and structure-dependent properties of all known nanomaterials.

Because of their unique properties, carbon nanotubes have attracted significant attention from researchers around the world and their use has been proposed for many applications. CNTs have not only excellent and diverse mechanical properties - tensile strength of 60–100 GPa (Troiani *et al.* 2003) and Young's modulus of 0.3–1.0 TPa (Yu *et al.* 2000) - but also excellent thermal properties. The thermal conductivity of a single nanotube can be as high as 6600 $W \cdot m^{-1}K^{-1}$ (Berber *et al.* 2000), which is due to ballistic phonon transport. SWCNTs also have interesting optional semiconducting/metallic electrical behaviour (Yorikawa & Muramatsu 1995, Kleiner & Eggert 2001). The electronic properties of carbon nanotubes depend mostly on the chirality (*i.e.* the chiral angle between carbon hexagons and the tube axis) and the type of nanotube. Practically all MWCNTs show metallic behaviour at room temperature due to their large diameter, which causes the band gap to be small. On the other hand, SWCNTs can be either metallic or semiconducting depending on their chirality. Statistically, 1/3 of SWCNTs are metallic and 2/3 of them are semiconducting. The chiral vector ($c_h$) is defined on a hexagonal lattice as

$$c_h = n\bar{a}_1 + m\bar{a}_2, \quad (1)$$

where $\bar{a}_1$, $\bar{a}_2$ are unit vectors, and n, m are integers. The chiral angle ($\theta$) is measured relative to the direction defined by $\bar{a}_1$ (Figure 2). There are three different chiralities in nanotubes: armchair, zigzag and chiral. Armchair nanotubes show metallic conduction because the valence and conduction bands overlap each other at the Fermi level. Zigzag and chiral nanotubes can be either metallic or semiconducting. Zigzag CNTs ($m = 0$) are metallic when n is a multiple of three. Chiral CNTs are metallic when

$$2n + m = 3q, \quad (2)$$

where q is an integer. In Figure 2a, a diagram has been constructed for (n, m) = (2, 1) and the unit cell of the nanotube is bound by OAB'B. To form the nanotube, this unit cell is rolled up so that O meets A and B meets B'. Different types of carbon nanotube have different values of n and m (Figure 2b). Zigzag nanotubes

correspond to (n, 0) and have a chiral angle of 0°, armchair nanotubes have (n = m) and a chiral angle of 30°, while chiral nanotubes have general (n, m) values and a chiral angle of between 0° and 30°.

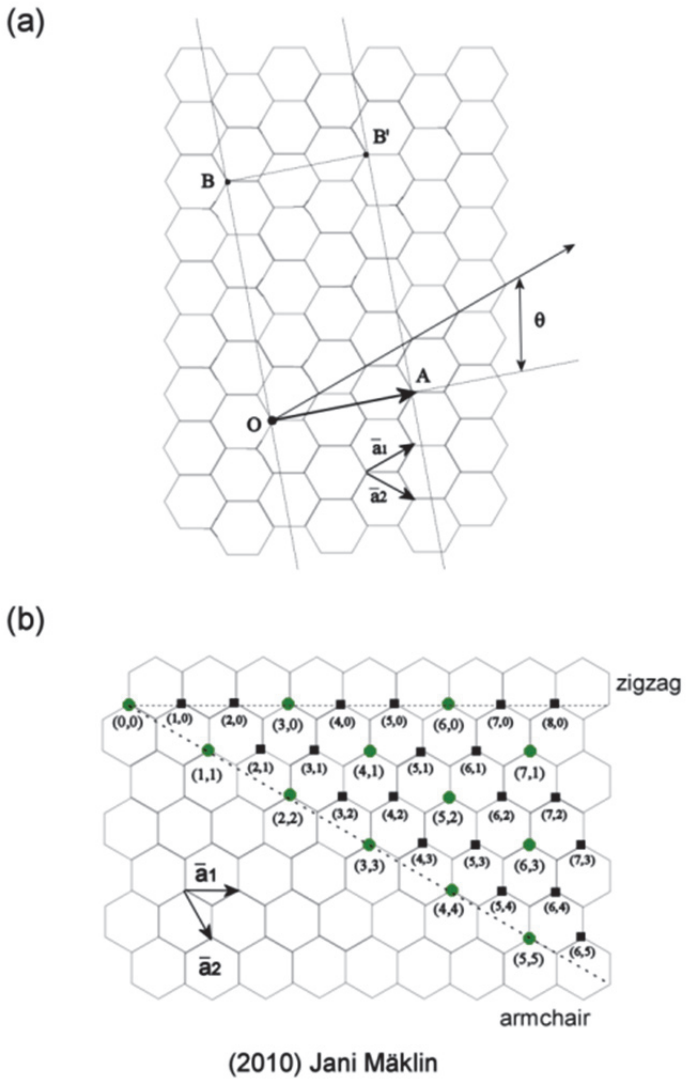


**Fig. 2. Carbon nanotube presented as two-dimensional graphene sheet. a) Definition of unit vectors and chiral angles are defined. b) The different types of carbon nanotubes.**

Due to these exciting properties, CNTs have been proposed as potential candidates in various applications, such as interconnects (Close *et al.* 2008, Cassell *et al.* 2003), gas sensors (Valentini *et al.* 2003, Li *et al.* 2003), electrical contact brushes (Paper III) and solar cells (Kongkanand *et al.* 2007). They have also been demonstrated for use as thermal interface material (TIM) (Hu *et al.* 2006, Zhang *et al.* 2008). In addition, CNTs have been predicted and demonstrated to have attractive properties for thermal management applications (Hone *et al.* 1999, Pop *et al.* 2006). Combining this with their numerous other excellent properties such as light weight, large specific surface area, excellent mechanical strength, high aspect ratio, flexibility and anisotropic thermal diffusivity/conductivity (Ivanov *et al.* 2006, Borca-Tasciuc *et al.* 2005) they are ideal candidates for thermal management applications in electrical components and devices (Kordás *et al.* 2007, Fu *et al.* 2012) as well as in polymer composites (Ni *et al.* 2012). To summarize, carbon nanotubes have been intensively researched for various applications and the research has increased dramatically during the last decade (Figure 3).

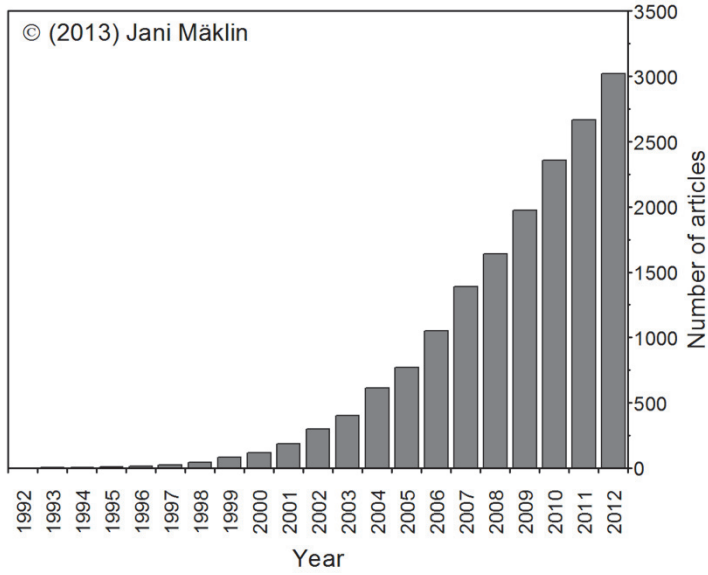


**Fig. 3. Number of publications found in Thomson Reuters Web of Knowledge using keywords "carbon nanotube AND application". Search was performed on 18.06.2013.**

## 1.2 Objective and outline of the thesis

The objective of the thesis was to implement and integrate carbon nanotubes into electrical assemblies using existing technologies in order to demonstrate feasible applications, such as gas sensors, electrical brush contacts and cooling fins.

In Chapter 2, gas sensors based on CNT-inks were made and their sensitivity towards nitric oxide (NO) examined. Both MWCNT- and SWCNT-based gas sensors are used in synthetic air and argon (Ar) buffers and the performances of such sensors were compared. SWCNT-based gas sensors were found to outperform their MWCNT counterparts due to the tuneable Fermi-level in semiconducting nanotubes. Moreover, the possible enhancement in selectivity of CNT-based gas sensors using fluctuation enhanced sensing (FES) and pattern recognition methods was investigated.

In Chapter 3, the electrical properties of inkjet deposited CNTs were studied by measuring the output and transfer characteristics of nanotube films having different surface coverage on alumina and silicon chips, respectively. Chapter 4 describes how robust CNT forests could be used as a new and superior alternative to traditional electrical contact brushes. Their outstanding mechanical flexibility accompanied by excellent electrical properties were exploited in CNT-based brush contacts that outperformed traditional macroscopic solid contact materials.

In Chapter 5, the thermal properties of robust, freestanding MWCNT forests were studied. Thermal diffusivity of the forests was measured by using a flash method and the effective thermal conductivity was derived from the measurement results. MWCNT films were found to outperform ordinary thermal interface (TIM) materials and were concluded to be potential alternatives for replacing Al and Cu components in thermal management applications (heat removal/dissipation). In addition, the good thermal properties of the aligned nanotube films were exploited in a chip cooling application, where CNT pillar structures were solder-mounted on ceramic chips and used as efficient heat sinks. The integrated CNT based coolers showed similar performance to that of Cu-based heat sinks, suggesting that the technology is feasible for the production of carbon based coolers in ceramic packages.

# 2 Carbon nanotube gas sensors

Their small size, large specific surface area and the change of electrical conductivity upon exposure to gaseous molecules are all beneficial for the application of carbon nanotubes as gas sensing materials. Nitrogen oxides, such as nitrogen monoxide (NO) and nitrogen dioxide ($NO_2$), are typical air pollutants that cause environmental problems. Also, in the medical field there are demands for small and cheap gas sensors for NO detection. NO has been used as a non-invasive marker for airway inflammations and is an important biomarker in asthma and other respiratory disorders (Liu & Thomas 2005, McCurdy *et al.* 2007). In this chapter, SWCNT and MWCNT based resistive gas sensors are characterized and their sensitivities towards NO gas are compared. The effects of buffer gas, NO gas concentration and measurement temperature on the resistance of CNT films are discussed.

## 2.1 Background

Adsorbed oxidative gas molecules, such as $NO_x$, shift the Fermi level in the nanotubes closer to the valence band, causing an enhancement of hole-transport in the nanotubes. Thus, the resistance of nanotubes is decreased. This effect is more pronounced in an air buffer environment for the following reasons. Firstly, oxygen molecules cause rearrangement of the local electronic density of states inducing a decrease in resistance (Collins *et al.* 2000). Secondly, as a consequence of the absorption and subsequent reaction of NO molecules with $O_2$, a number of different oxygen containing surface compounds such as $NO_2$ and $N_2O_4$ are likely to form on the nanotubes, thus increasing their conductance. With reductive gas molecules such as $H_2$, the valence band is shifted away from the Fermi level which results in hole depletion and a corresponding decrease in electrical conductivity (Kong *et al.* 2000). These doping effects are similar in both semiconducting and metallic nanotubes (Varghese *et al.* 2001). It is not just the nanotubes that are doped by adsorbed gas molecules but also the nanotube–electrode contacts, especially with SWCNTs as the semiconducting nanotubes form a Schottky contact with the metallic electrodes and semiconducting CNTs. This metal–semiconductor interface is similarly susceptible to variations in gas atmosphere.

The most common electrical gas sensors are resistive devices, referred to as Taguchi sensor, where only the conductance/resistance of the device is measured.

The major benefits of this sensor type are excellent sensitivity, short response time, low cost and easy implementation, relatively easy manufacturing and suitability for portable instruments. However, the Taguchi sensor has a major drawback; it usually lacks selectivity. In many cases, the sensors can be made very sensitive but they tend to respond to any kind of moiety. This is very problematic, especially in gas mixtures where both types of gases, oxidative and reductive, are present. Several methods have been presented to overcome this selectivity problem. The easiest way is to use a sensor array (Lu *et al.* 2006, Star *et al.* 2006), where individual sensors have different active materials and thus are more sensitive to particular analytes. Typically, a map of sensor responses is constructed and the data is further analysed by pattern recognition methods, such as principal component analysis (PCA) and linear discriminant analysis (LDA).

### *2.1.1 Fluctuation-Enhanced Sensing*

One way of increasing the selectivity without changing the material is to measure a different property of the sensor, e.g. the noise generated in the of sensor's resistance instead of the resistance value itself. The measured noise is useless itself as the information is "hidden" within it. However, using appropriate analysing (pattern recognition) methods such as PCA or LDA, the hidden information can be extracted. Carbon nanotubes have been proven to be good candidates for this type of sensing (Haspel *et al.* 2008) since the porous, high aspect-ratio structure of CNTs generates more noise than bulk, crystalline materials.

In general, fluctuation-enhanced sensing (FES) is based on the fact that stationary fluctuations of a system carry specific information about the system itself (Bruschi *et al.* 1994, Kish *et al.* 2000). Typically, low-frequency noise (1/f noise) is measured across the CNT-based resistive gas sensor and further analyzed. The measured noise voltage is the sum of two parallel 1/f noises coming from the gas sensor and the parallel reference resistor, respectively. The parallel resistor should be a precise low-noise metal film resistor with a resistance value close to that of the gas sensor. Typically, the noise level of the gas sensor is orders of magnitude higher than that of the parallel reference resistor. The power spectral density (PSD) of the measured noise is used for the analysis, which is done using the PCA method. FES has been shown to be an excellent method for gas sensing when using carbon nanotubes as the sensing material (Haspel *et al.* 2008). The schematic of the PSD measurement system is shown in Figure 4.

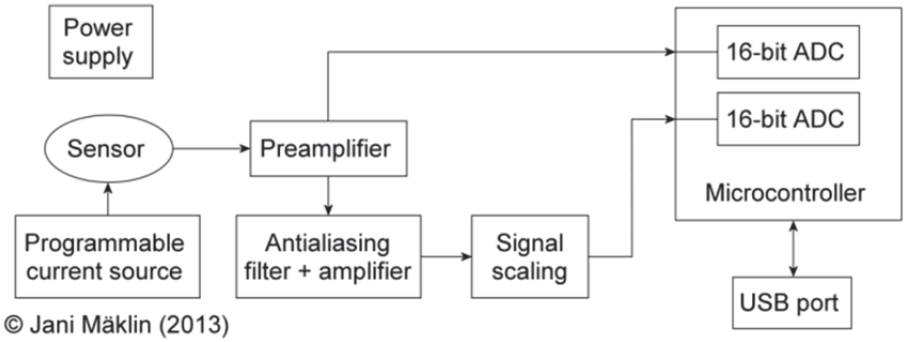


**Fig. 4. Block diagram of the PSD measurement system.**

PCA is a mathematical procedure that uses an orthogonal transformation to convert a set of variables into a set of uncorrelated variables called principal components. Basically the method reduces dimensions so that the resulting variables contain the most possible information of the system. In practice, the measured PSD of 1/f noise is mean centred and the line frequency (50 Hz) and its harmonics are filtered out. The noise measurement system is embedded into the gas measurement setup and the whole measurement is PC–controlled using a custom LabVIEW program. In the measurements the PSD of the noise is measured and transferred to the PC using a USB connection. This USB connection is used not only for communicating but also for powering the noise measurement circuit boards. PCA calculations are performed afterwards using MATLAB routines (embedded into custom LabVIEW measurement software).

In temperature modulated sensing (TMS), the sensor is temperature programmed or modulated during the measurements to achieve better selectivity (Lee & Reedy 1999). The temperature modulation of the sensor alters the adsorption and desorption kinetics of the gas molecules and, as all the gases have their own characteristic kinetics behaviour, the gases can be better distinguished. This method shares the same drawbacks of extra electronics and costs as previously mentioned methods.

## 2.2 CNT-based gas sensors

CNT-based gas sensors have been shown to exhibit fast response time, good sensitivity and low temperature operation (below 200 °C). On the other hand, the

two main drawbacks are the slow and incomplete recovery of the sensor and poor selectivity. These drawbacks are due to same reasons that give the devices their high sensitivity; a porous tubular structure with large specific surface area which provides plenty of sites for gaseous molecules to be adsorbed. A typical reported recovery time is several hours (Kong *et al.* 2000, Li *et al.* 2003). There have been various attempts to overcome this limitation. Suehiro *et al.* (2006) used ultraviolet light to knock the adsorbed gas molecules out of the CNT sites; also heating up and degassing the sensor in a vacuum are frequently used to desorb gas molecules from the surface (Kong *et al.* 2000). Although sensor recovery can be improved through these methods they are still not efficient enough or are simply impractical for real-life applications. Poor selectivity has mainly been addressed by doping and decoration with metals and their oxides (Penza *et al.* 2007, Star *et al.* 2006). In early studies, nanotubes were either directly grown on a specific surface or the studies focused on isolated individual nanotubes. However, as the chemistry of nanotubes has been explored and improved so the diversity in methods of fabrication of CNT-based sensors has become broader. Different deposition techniques such as inkjet-printing (Mustonen *et al.* 2006) have enabled more practical concepts in sensor fabrication.

There is a difference in chemical sensor performance between SWCNTs and MWCNTs; SWCNTs are more sensitive to changes in chemical environment than MWCNTs, mainly because of the more considerable change in the density-of-states around the Fermi level. Since the band gap in carbon nanotubes is inversely proportional to nanotube diameter, SWCNTs exhibit larger band-gaps than those of MWCNTs (Dresselhaus *et al.* 2004). Moreover, as SWCNTs can be either metallic or semiconducting, they can form metal–metal, metal–semiconductor, or semiconductor–semiconductor junctions.

The sensing performances of nanotube networks of SWCNTs and MWCNTs towards NO [50 ppm] in air and argon buffers are presented in Table 1 (Paper I).

**Table 1. Sensor responses of CNT gas sensors towards 50 ppm NO with different buffer gases.**

| Nanotube type | Gas atmosphere | Sensor response (%) |
|---|---|---|
| SWCNT | NO in argon | 13 |
| SWCNT | NO in air | 30 |
| MWCNT | NO in argon | 1 |
| MWCNT | NO in air | 3 |

It is clear that when designing a gas sensor based on nanotubes, SWCNTs are better candidates from the sensitivity point of view. And even though individual nanotubes outperform CNT networks (films, forests) in sensitivity, using films of nanotubes (networks, bundles) it is easier to fabricate sensors having similar sensing properties. This is due to the fact that all nanotubes exhibit unique properties that can be very different from each other but in networks or bundles of nanotubes, these properties are averaged out.

## 2.3 Resistive nitric oxide gas sensors based on CNTs

Stable solutions of carboxyl functionalized SWCNTs and MWCNTs enable printing as well as drop-casting of nanotube films on various substrates. Both methods have been proven to be relatively easy and cost-effective ways to fabricate gas sensors based on nanotubes (Mustonen *et al.* 2006) (Mäklin *et al.* 2008).

In this work, drop-cast CNTs from aqueous dispersions were applied on alumina based sensor chips. The structure comprised of two gold (Au) electrodes with a gap of ~200 µm, while on the reverse side screen-printed thick-film integrated platinum (Pt) heater was applied to enable temperature modulation (Figure 5).

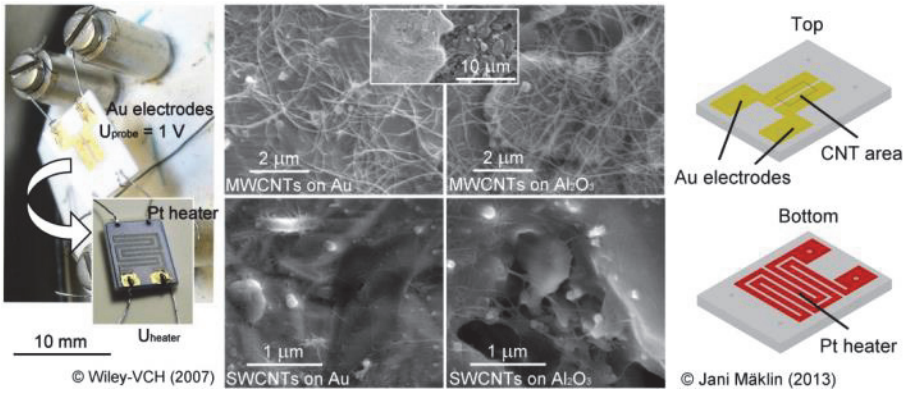


**Fig. 5. CNT-based gas sensor fabricated on a 635 µm thick alumina substrate. Left panel: Gas sensor (size of 16.9×6.3 mm$^2$) with thick film gold electrodes (front side) and integrated platinum heater (back side). Middle panel: FESEM images of drop-cast carbon nanotube gas sensing layers deposited on the thick-film electrode structure. The upper images show the tangled network of MWCNTs on a gold electrode (left) and**

**on the alumina surface between the electrodes (right). Inset: low-magnification micrograph of the edge of sensor electrode. In the lower images, a corresponding sensor made of SWCNTs is shown. Right panel: Schematic drawings of both sides of the sensor chip. (Paper I, published by permission of Wiley-VCH).**

The gas sensing measurements were performed in a gas chamber of 500 mL in volume. The sensors were exposed to NO gas (1–100 ppm) using argon or synthetic air as buffer at measurement temperatures between 25 and 100 °C. The sensors were probed with a constant voltage (1 V) while the electrical current through the devices was measured. Resistance versus gas concentration, exposure time and temperature characteristics were analyzed. The recovery of sensors after each measurement was achieved by heating to 150 °C using the integrated Pt heating circuit. This recovery temperature was chosen to maintain the functionalization in the nanotubes, viz. at higher temperatures a sensor "reset" may cause a decarboxylation or other changes in the chemical functionalization and possibly ruin the sample (Datsyuk *et al.* 2008). As found in previous gas exposure experiments, the time needed for sensor recovery varied from 5 to 15 minutes. However, no perfect sensor recovery was achieved. This incomplete recovery was more pronounced in higher gas concentrations measurements and could probably be attributed to the relatively low recovery temperature used in the experiments.

The relative change in the resistance of the sensors ($\Delta R/R_0$) was investigated as a function of exposure time, NO concentration, temperature, and carrier gas chemistry (Figure 6). A drop of the CNT film resistance upon NO exposure was observed for all sensors. The sensor saturation was found to be fairly independent of the gas concentration in the investigated range (10–100 ppm); however the change of $\Delta R/R_0$ was faster for higher NO concentrations. This indicated an NO adsorption mechanism on the nanotubes' surface in which the substrate coverage is not influenced significantly by desorption of adsorbed NO, i.e. the equilibrium between the adsorption and desorption processes is shifted towards the surface-bond products. It is very likely that a strong binding is established between NO and the $sp^2$ hybridized electrons of the CNTs' outer graphene layer (Long & Yang 2001) as NO is a strong π–acceptor ligand (Shriver & Atkins 1999). The existence of a strongly bound NO–CNT product was also supported indirectly by the very slow sensor recovery without heating as shown in Figure 5c–d. (Paper I).

Depending on the gas carrier chemistry, the resistance of the SWCNT sensors decreased by ~40% and ~12% for air and argon buffers, respectively. For MWCNT sensors, the corresponding values were significantly lower (<10 % in

synthetic air buffer and <1 % in argon buffer). The decrease of resistance upon NO exposure is a consequence of the oxidative environment in which hole-transport in the nanotubes is enhanced through a lowered Fermi-level (Yamada 2004, Avouris & Chen 2006). This effect is, as expected, more pronounced in air buffer due to the presence of the oxygen molecules in air which causes the earlier explained rearrangement in the local electronic density of states. Also, reactions between NO and $O_2$ molecules cause nitrogen dioxide ($NO_2$) to be present in the system.

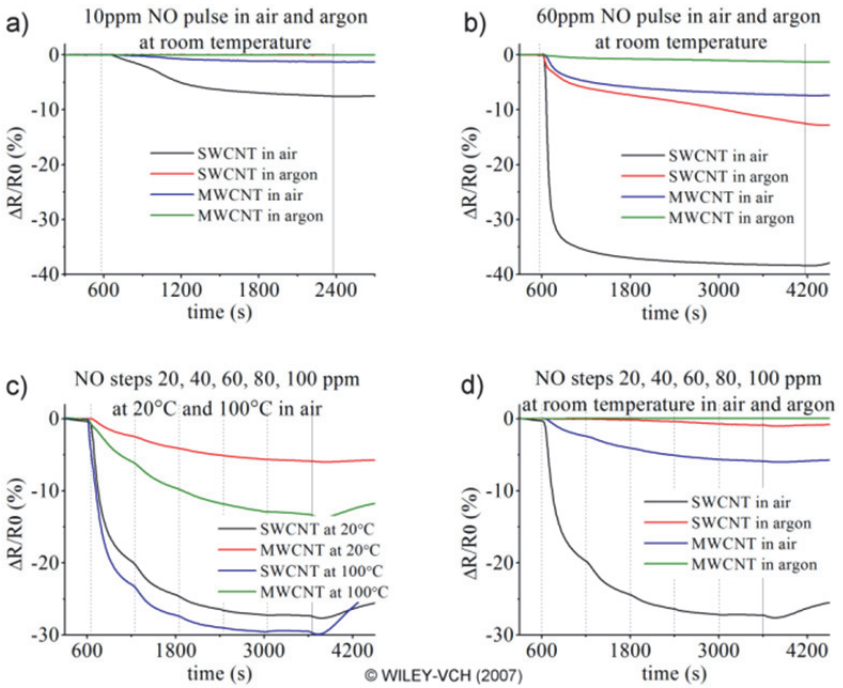


**Fig. 6. Measurements with different gas concentrations, exposure time and temperature. Vertical lines denote the injection of NO pulses (dashed lines) and annealing at 150 °C (solid line). In a) and b) sensors were exposed to a constant pulse of NO of 10 ppm and 60 ppm at room temperature in synthetic air and argon carrier gases, respectively. In c) and d) the NO pulses were fed by increasing the concentration of NO in the carrier gas followed by annealing at the end of pulses. c) The effect of temperature in synthetic air. d) The comparison between carrier gases at room temperature. In all measurements initial pre-flushing (600 s) of chamber was performed with the corresponding carrier gas before NO feeding (Paper I, published by permission of WILEY-VCH).**

In addition, repeatability and sensor drift were studied by subsequent exposure–cleaning cycles (Figure 7). In these cycling measurements, the sensors were exposed to repeated gas pulses – each followed by a cleaning cycle, i.e. heating to 150 °C for 10 minutes.

In all experiments, the sensors with SWCNTs outperformed their counterparts with MWCNTs. This result is consistent with the larger band-gap in SWCNTs, which is modulated locally by the adsorbed gaseous molecules on the surface.

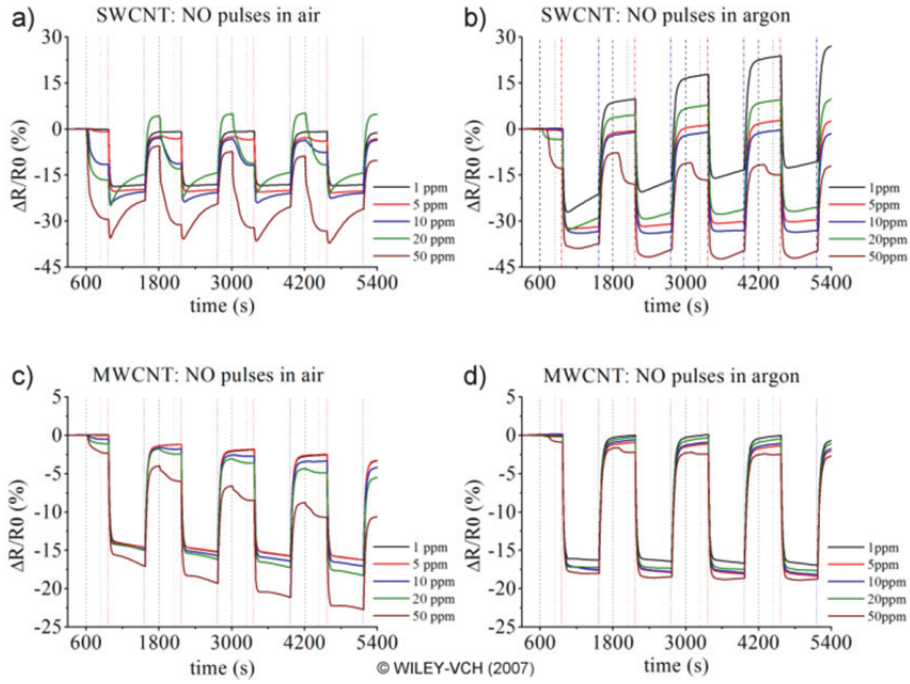


**Fig. 7. Repeatability and sensor drift measurements. Before pulse measurements initial pre-flushing (600 s) was performed. Pulse sequence is as follows (shown by vertical lines): NO pulse in carrier gas (240 s, black dashed line), flushing with carrier gas (120 s, black dotted line), annealing at 150 °C (600 s, red dash-dot line) followed by cooling (240 s, blue dash-dot line) before next pulse (Paper I, published by permission of WILEY-VCH).**

Due to the good work function matching, the role of the contact between semiconducting nanotubes and gold electrodes seemed to have no (or at least negligible) effect on the conduction (Zhao *et al.* 2002, Yang *et al.* 2005, Park & Hong 2005). This can be concluded from the measured *I–V* characteristics (Figure

8). The *I–V* measurements were carried out by sourcing current (from 1 nA up to 20 mA) while measuring voltage using a Keithley 2612 dual channel SourceMeter, which was controlled by a custom LabVIEW code. The results showed that the fabricated devices were acting as linear ohmic sensors, i.e. the *I–V* curves were linear in the measured range and the slopes of the curves were changing according to the introduced gas atmosphere.

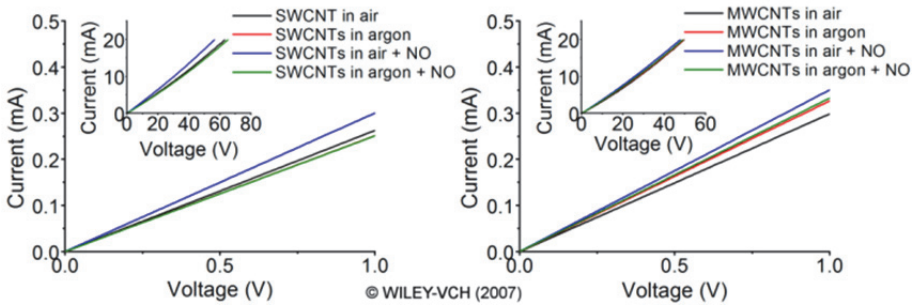


**Fig. 8. *I–V* measurements from the SWCNT (left) and MWCNT (right) sensors with and without NO gas (50 ppm) in synthetic air and argon carrier gases. Insets show linear response over the whole measured range (Paper I, published by permission of WILEY-VCH).**

# 3 Electrical characterization of printed SWCNT films

Electronic transport properties of inkjet-printed single-walled carbon nanotubes were studied using a customized semi-automated measurement system allowing convenient, reliable and fast characterization of the nanotube films.

## 3.1 Background

Printed electronics is a research area that has gained significant attention during recent years from researchers all over the world. Therefore it is natural that carbon nanotubes have also been exploited in printed electronics. Printed CNTs have been utilized for various electrical applications such as transistors (Beecher *et al.* 2007, Vaillancourt *et al.* 2008, Mehlich *et al.* 2012), OLEDs (Chen *et al.* 2011) and interconnects (Tawfick *et al.* 2009). The electrical transport mechanism of nanotubes is influenced by many factors, including nanotube chirality (Yorikawa & Muramatsu 1995, Kleiner & Eggert 2001), temperature (Ebbesen *et al.* 1996), doping/chemical functionalization (Choi & Yu 2012, Ionescu *et al.* 2012) and electrical contacts (Avouris 2002). The electrical transport properties of SWCNTs can be deduced from the properties of a graphene sheet. In carbon nanotubes, electrons propagate along a conjugated electron cloud within a crystal having no dangling bonds on its surface (in a defect free nanotube) resulting in ballistic electron transport over a distance of a few micrometres (Mann *et al.* 2003). In semiconducting SWCNTs, the band-gap is inversely proportional to nanotube diameter. Moreover, semiconducting SWCNTs form Schottky contacts when contacted with metals or metallic nanotubes (Avouris 2002). In MWCNTs the situation is more complex as each wall can have different chirality. However, the studies have shown that electrical transport is dominated by the outermost wall exhibiting a quasi-ballistic conduction mechanism (Schönenberger *et al.* 1999, Bachtold *et al.* 1999). In principal, MWCNTs behave as metallic conductors except for their temperature coefficient of resistance, which can be negative (Bockrath 1999, Naeemi & Meindl 2007). In SWCNT networks (bundles or films of SWCNTs) – because of the mixture of nanotubes with different band structures - conduction mechanisms such as hopping of charge carriers (Kaiser *et al.* 2001) and carrier injection through Schottky junctions between metallic and semiconducting nanotubes (Stadermann *et al.* 2004) take place making the overall picture of carrier transport even more complex than in homogeneous materials.

In spite of these factors, bundles and/or large network configurations can be expected to average out any variations in the above mentioned parameters. Devices fabricated from such structures can be expected to remain more "reproducible" in their properties and performance, with higher throughput, thus it could be in some cases even more favourable to use bundles/networks in applications. Since in many applications the dimensions of electrodes are much larger than the diameter of individual nanotubes, scaling up the active elements between the electrodes using bundles and/or networks serves to enhance device–to–device reproducibility, in comparison to individual nanotubes, without compromising the overall device size (Paper II).

## 3.2 Printed SWCNT films

Aqueous solutions of nanotubes were deposited by inkjet-printing (Dimatix DMP-2831 materials printer) on alumina and silicon (Si). In both types of sample the chips had an integrated (platinum) heater for measurements at elevated temperatures. In alumina samples, SWCNTs were deposited between two thick-film gold electrodes with a gap of ~200 µm (Figure 4, chapter 2) while the Si chips consisted of 4–probe composite Ti/Pt electrodes of 6 µm × 75 µm (width × length) with a 15 µm gap in between (Figure 9). By printing different numbers of layers (3–20) of nanotube ink over the same pattern, nanotube films with different surface coverage were achieved (Mustonen 2009).

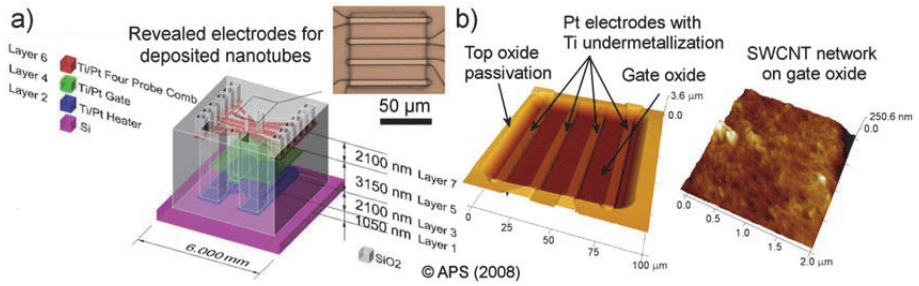


**Fig. 9. (a) Layout of the Si chip used in the CNT thin film FET measurements. The optical micrograph shows a set of Pt electrodes (source–drain) upon which the nanotube films were printed. NOTE: The z-axis scale is exaggered. (b) Atomic force microscopy images of the electrode area. The higher magnification image shows a network of nanotube bundles printed between the electrodes (Paper II, published by permission of American Physical Society).**

## 3.3 Electrical characterization

Current–voltage (*I–V*) characteristics for alumina samples were measured on each sample with a dual channel SourceMeter (Keithley 2612) in ambient air and in nitrogen atmosphere at temperatures from 20 to 150°C. A custom LabVIEW code was developed for controlling the measurement device and for extracting data for analysis (Appendix 1). As mentioned in Chapter 2, due to the good work function matching, the contact between semiconducting nanotubes and Au electrodes (alumina samples) had an insignificant effect on the *I–V* characteristics. This is crucial, especially with low density nanotube films (low surface coverage), since a Schottky interface is formed between the metal and individual semiconducting nanotube(s). The Schottky interface would cause thermal emission to be the dominant conduction mechanism at room temperature and above (Avouris & Chen 2006, Appenzeller *et al.* 2004, Sze 1981). To demonstrate the existence of the Schottky contacts in the low density nanotube films, the printed nanotube networks were measured on FET silicon chips.

### *3.3.1 Alumina test chips*

The current–voltage (*I–V)* characteristics measured for the nanotube films deposited on alumina substrates are presented in Figure 10a–b. (Paper II, Mustonen 2009). The thick (i.e. high density) nanotube films behaved as ohmic conductors exhibiting linear *I–V* curves. This is a consequence of direct contacts between metallic SWCNTs that allow a continuous and highly conductive path for the current to flow through the nanotube film. The slopes of the *I–V* curves of the high density films were proportional to the number of printed layer repetitions (i.e. the nanotube surface coverage). In contrast, the thin (i.e. low density) nanotube films showed nonlinear *I–V* characteristics because the probability for formation of continuous metallic nanotube paths in the network was low due to the small amount of metallic nanotubes present in the film. That is why processes other than ohmic (typically nonlinear) conduction contribute to the current transport in the low density SWCNT film. These nonlinearities in output characteristics are hardly explained by self-heating since such an effect would be more pronounced for the high density films where significantly higher powers (currents) are generated compared to the low density films (Paper II).

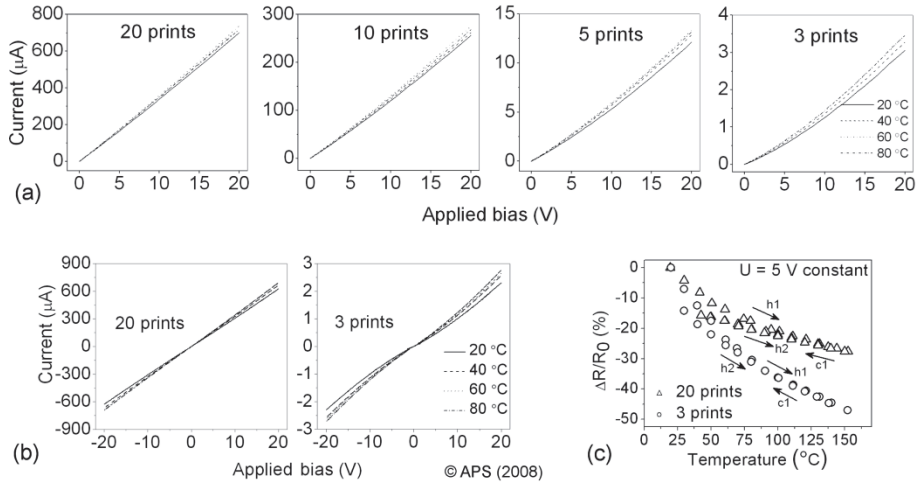


**Fig. 10. Current–voltage characteristics of inkjet deposited SWCNT films of various print repetitions (surface coverage) in the temperature range of 20 to 80°C measured (a) in ambient air and (b) in nitrogen atmosphere. (c) Relative change of film resistance of dense (20 prints) and sparse (3 prints) networks upon heating (h1) and subsequent cooling (c1) and re-heating (h2) in nitrogen atmosphere up to 150°C (Paper II, published by permission of American Physical Society).**

To examine the temperature dependency of the sample resistance the samples were measured in a nitrogen atmosphere using a constant bias of 5 V (Figure 10c). The drop in resistance of the low density film with increasing temperature was found to be higher than that of the high density nanotube film – probably due to the exponential dependence of Schottky emission on temperature (Fischer *et al.* 1997, Kaiser *et al.* 1998, Skákalová *et al.* 2006). Furthermore, a negative temperature coefficient of resistance is expected for such low-density nanotube films. In the case of the high density films, there are two processes involved: firstly, electron–electron interactions in short m-CNTs that can cause a very low negative temperature coefficient of resistance (Bockrath 1999), and secondly, carrier scattering on radial breathing mode (RBM) phonons in long metallic SWCNTs that can show a positive temperature coefficient of resistance (Rinzler *et al.* 1998, Gaál *et al.* 2000, Hartschuh *et al.* 2003). A combination of these two processes results in a lower negative temperature coefficient of resistance for the denser films because, as the network becomes denser, more m-CNTs are

contributing to the current transport in the SWCNT network (Paper II, Mustonen 2009).

In addition to the intrinsic properties of nanotubes, the adsorbed molecules that are present on the nanotube films also need consideration when measuring CNT-based devices in ambient atmosphere. Electron donors or proton acceptors that are adsorbed on nanotubes increase the electrical resistance because of the induced downshift of the valence band of the p-type nanotubes away from the Fermi-level by which hole depletion occurs and consequently the electrical conductivity is decreased (Kong *et al.* 2000, Paper II). To reveal the effect of adsorbed species on the output characteristics of the samples, the resistances of both types of sample were measured not only while heating up but also while cooling the samples back to room temperature in the same inert atmosphere ($N_2$). Both $\Delta R/R_0$ *vs.* $T$ curves split at ~100 °C and showed lower resistance values in the cooling ramp than during the heating step. While heating up the samples again the resistance of the samples followed the values obtained in the previous cooling ramps. The results suggest the presence of strongly adsorbed water on the nanotubes, which desorbed during the first heating cycle (Paper II, Mustonen 2009).

The picture is even more complex for carboxyl functionalized nanotubes because not only the adsorbents on the nanotubes but also the functional groups and the adsorbed molecules upon them change the local distribution of charge carriers (Dettlaff-Weglikowska *et al.* 2005, Balasubramanian & Burghard 2005). Covalently bonded carboxyl functional groups increase the conductivity of the nanotubes due to the strong electron-withdrawing property of the functional group; namely a partial positive charge appears around the carbon atom of the backbone that bonds the carboxyl group. Upon water exposure a reduced electron-withdrawing power of the oxygen-containing defect groups leads to a reduced hole carrier concentration and consequently increases the resistance in the p-type nanotubes (Watts *et al.* 2007, Paper II).

In SWCNT films, the current carrying network consists of both metallic and semiconducting nanotubes (these can be referred to as wires). As already mentioned in Chapter 1, statistically the quantity of semiconducting nanotubes is twice that of the metallic ones (Avouris & Chen 2006, Fuhrer *et al.* 2000). In SWCNT films, a random sequence of both semiconducting (s-CNT) and metallic carbon nanotubes (m-CNT) forms the current conduction paths. Junctions between two similar nanotubes (s-CNTs or m-CNTs) have high conductance, and are ohmic but in the case of two dissimilar nanotubes (s-CNT + m-CNT), a

rectifying Schottky barrier (contact) is formed because the valence band edge in s-CNT lies below the Fermi level of m-CNT (Fuhrer *et al.* 2000). In low density films, only a few contiguous conduction paths exist and the probability for Schottky barrier formation is increased. In a simple picture, carriers that have energy larger than the barrier height will be injected via thermionic emission into the nanotube. In this picture, for a metal–semiconductor interface, the potential and temperature dependent current density $J(V,T)$ is described as (Sze 1981):

$$J(V,T) = A^* T^2 \exp\left(-\frac{\Phi_b}{kT}\right)\left[\exp\left(\frac{qV^*}{kT}\right)-1\right], \tag{3}$$

where $\Phi_b$ is the Schottky barrier height, $A^* = 4 \cdot \pi \cdot q \cdot m^* \cdot k^2/h^3$ is the Richardson constant, $q$ is the elementary charge, $m^* = 0.037 \cdot m_e$ is the effective mass of the carriers (Jarillo-Herrero *et al.* 2004), $k$ and $h$ are Boltzmann's and Planck's constants, respectively. The voltage drop on the series intrinsic resistance, $R$, of the nanotubes is considered by writing $V^* = V - RI$, where $R$ is the inverse of the $I$–$V$ slope at large biases. Applying Equation 3 for a CNT layer having an average cross-section ($A$) and a number of junctions ($m$) via the percolated path, the current $I$ can be expressed as (Paper II, Mustonen 2009):

$$I(V,T) = AA^* T^2 \exp\left(-\frac{\Phi_b}{kT}\right)\left[\exp\left(\frac{q(V-RI)/m}{kT}\right)-1\right]. \tag{4}$$

The parameters $\Phi_b$ and $m$ were resolved by fitting Equation 4 to the measured $I$–$V$ plots. The obtained barrier height values – plotted in Figure 11 – were in good agreement with the measured values for individual junctions of metallic and semiconducting nanotubes (Yao *et al.* 1999, Fuhrer *et al.* 2000). Furthermore, the calculated average barrier height gradually decreased, together with the number of Schottky junctions being involved in a percolation path, with increases in the number of printouts. Moreover, increased surface coverage and film thickness were also achieved and as a result of this most charge carriers could see a reduced effective Schottky barrier, which gave rise to pronounced linear $I$–$V$ curves. It was also noted, that there was a big jump in channel conductivity between 5 and 10 printouts. This indicates a critical percolation threshold, i.e. a critical number of nanotubes are present in the nanotube network that enables a contiguous ohmic-type conduction path for charge carriers. After the percolation threshold has been reached, the Schottky junctions have a less dominant effect on the current carrying properties. As Fuhrer *et al.* (2000) has shown, an ohmic path can consist

of either purely m- or s-CNTs but if the channel consists of a mixture of these two types of nanotubes then Schottky junctions are formed.

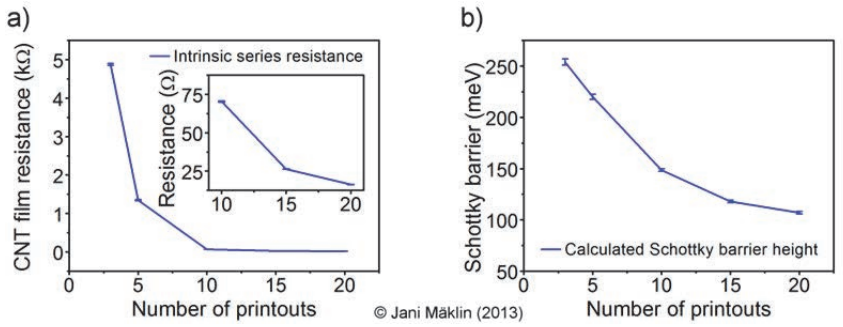


**Fig. 11. Intrinsic series resistance (a) and effective Schottky barrier height (b) plotted as a function of number of printouts. (Paper II, Mustonen 2009).**

### *3.3.2 Silicon test chips*

The formation of Schottky junctions pins the valence band of semiconducting CNTs close to the Fermi level of the metallic counterpart (Fuhrer *et al.* 2000). Application of a gate voltage causes band-bending near the contacts, which can modulate the effective energy barrier visible to the injected charges, thus controlling the channel conductance and giving rise to the well-known p-type transistor behaviour in pristine semiconducting carbon nanotubes. To examine the role of Schottky junctions on output characteristics in the SWCNT films, FET-devices with a bottom gate configuration ($SiO_2$ gate oxide thickness ~3 μm) were fabricated on silicon chips. The effect of external electric fields on the transport characteristics of the SWCNT films exhibiting different thicknesses was also studied.

As expected, low density films showed nonlinear *I–V's* that could be modulated with applied gate voltage (Figure 12a) with a corresponding on–off ratio of up to ~10. The achieved on–off ratio could be further improved by using high-κ dielectric gate oxides. The large hysteresis in the $I_{S-D}$ *vs.* $U_G$ curves suggests considerable charge injection of carriers into the surrounding dielectric. On the other hand, a chip with a high density and well conducting nanotube film exhibited linear *I–V* characteristics and had no gate response, in agreement with the metallic nature of such films (Figure 12b) (Mustonen 2009).

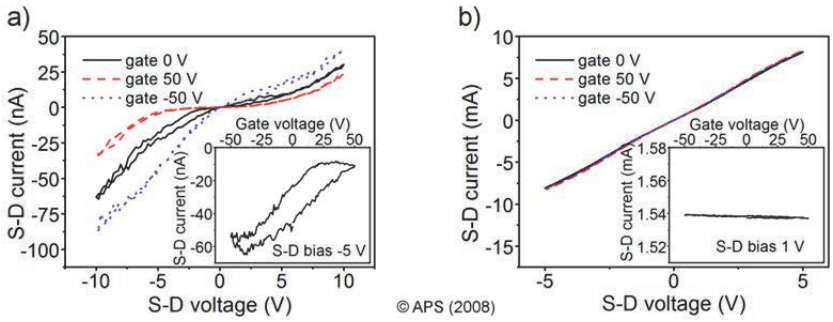


**Fig. 12. $I$–$V_{SD}$ and $I$–$V_G$ sweeps performed on FET-devices having (a) low-density SWCNT network and (b) high-density SWCNT network as a channel (Paper II, published by permission of American Physical Society).**

# 4 CNT-based electrical brush contacts

Carbon nanotubes can be used not only in nanoscale applications but also in macroscopic applications. Robust, aligned MWCNT films are here presented as effective rotating and sliding electrical contacts. Both the mechanical and electrical properties of CNTs were exploited for fabricating such devices. AC and DC electrical properties of the MWCNT films were both investigated in combination with the applicability of such films for electrical contacts. The feasibility of such films as practical, durable and low-noise alternatives for conventional electrical contact brushes was demonstrated.

## 4.1 Background

Most of the research on the applications of carbon nanotube is currently concentrated on individual nanotubes or on deposited thin films. Not much interest has been directed towards macroscopic applications utilizing robust CNT films/forests although it has been reported that repeatability, i.e. the ability to fabricate devices having similar properties, is increased by the use of such forests. This is because the variations in the properties of individual nanotubes are averaged out, similarly to those in random thin films.

The unique intrinsic properties of individual carbon nanotubes have been exploited in nanoelectromechanical systems and nanoelectronic devices (Sazonova *et al.* 2004, Dujardin *et al.* 2005). Large area aggregates of vertically aligned CNT films (or brushes) can be synthesized directly by catalytic chemical vapour-phase deposition methods (Zhu *et al.* 2002) on substrates and separated from the substrate for applications. Such brushes can have a large foot-print area up to square centimetres and with thicknesses greater than several millimetres (Yun *et al.* 2006). Aligned CNT brushes have also been exploited in various applications such as super-capacitor electrodes (Talapatra *et al.* 2006), super-compressible springs (Cao *et al.* 2005), and chip-cooling elements (Kordás *et al.* 2007).

The most common applications for sliding electrical contacts are current-carrying contact brushes that are used in electrical motors and generators (Kuhlmann-Wilsdorf 1996). Electric motors with commutators and solid-type contact brushes are still widely used and desirable because of their intrinsically low magnetic fields, electrical noise and potential for high power density applications. The low cost, ease of speed control, and demonstrated operation

under a variety of challenging conditions are also key factors why brush contacts are so widely used in electric motors. In most devices, the brushes are fixed on flexible cantilevers that are designed ideally to provide compliance and low applied normal load but are yet able to follow the rotational error motions of the shaft without bouncing, an extremely detrimental process that leads to arcing and rapid brush deterioration (Kuhlmann-Wilsdorf 1996, Feng *et al.* 2007).

## 4.2 Electrical brush contacts with carbon nanotubes

CCVD grown MWCNT forests (Halonen *et al.* 2008) were used as sliding electrical brush contacts in conventional DC motors. MWCNTs were grown on patterned $Si/SiO_2$ templates (1000 nm thick thermal oxide, $10\times10$ $mm^2$ area). After the growth, the CNT forests were detached from the growth substrate by soaking the samples in EtOH:HF (7:3) solution followed by rinsing in ethanol and drying. To make the CNT brushes solderable and to enhance the CNT-cantilever interface properties, the forests were sputtered with Cr/Cu (50 nm/2 μm). The chromium acted as an adhesion layer for the CNT–copper interface and the copper enabled successful soldering. $1.8\times1.8$ $mm^2$ sized blocks were laser-cut from the freestanding films. The obtained MWCNT brushes were then soldered (~10 μm solder thickness) onto flexible brass cantilevers using a low melting point eutectic solder paste (46Bi–34Sn–20Pb, melting point of 96 °C).

Both DC and AC electrical properties of these contacts were investigated and the performance of the CNT brush contacts was compared to ordinary solid brush contacts made of carbon–copper composite (40–60 wt%). For better comparison of the noise levels, both types of contacts were brought into contact with the smooth rotating axle of an electric motor. This was done to obtain relevant data for contact resistance and electrical noise. In normal commutator type contacts it is very difficult to obtain this data due to the irregular structure of the commutator.

### *4.2.1 Electrical characterization of the MWCNT brushes*

The noise measurements were carried out with a current-stabilized source (10 mA, Keithley 6221) and the bias voltage was measured as a function of time with an oscilloscope (Agilent 53622A). The obtained noise data were processed with the OriginPro 8 built-in fast Fourier transform (FFT) analysis tool. The DC electrical (*I–V*) characterization was performed using a Keithley 6221 AC and DC current source in combination with a Keithley 2182A Nanovoltmeter. A custom

LabVIEW code (Appendix II) was used for controlling the devices and acquiring the measurement data for transmission to the PC. In the measurements the pulsed ramp sweep technique (3–point delta measurement) was used to reduce power dissipated while performing the sweep. This technique minimizes the heating of samples, which could otherwise skew the test results. The measurement technique was as follows; one measurement point was taken before each sourced pulse, one during each pulse, and one after each sourced pulse. With this procedure any thermoelectric EMF (i.e. Seebeck voltage) and moving offsets were cancelled out, leaving the true value of the voltage. In other words, pulsed measurement is a relative measurement which reduces the power used in measurements (and consequent heating of the DUT), thus making the measurements more precise.

The effect of the sputtered metal layers on both AC and DC electrical characteristics was investigated and compared with bare (un-sputtered) MWCNT brushes. DC measurements were performed on each sample by fixing them in between gold plate contacts (Figure 13a). Both types of sample showed linear *I–V* characteristics suggesting ideal ohmic behaviour in both cases.

AC impedance measurements were carried out with an RF impedance/material analyzer (Agilent E4991A) equipped with a parallel-electrode surface mounted device (SMD) test fixture using frequency sweeps up to 2 GHz (Figure 13c). A low-noise SMD resistor was used for validating the measurement setup and measurement results. The results were then fitted using the equivalent circuit shown in Figure 13b (for the reference resistor the circuit was different as it did not exhibit any capacitive component). The sputtered MWCNT sample behaved as a typical low-value resistor (similar to the reference SMD resistor) showing a small series lead inductance of ~475 pH at high frequencies (Figure 13b) and an additional stray capacitance of ~120 pF. For the bare CNT sample, the fitted lead inductance and stray capacitance values were ~2.1 nH and ~27 pF, respectively. Moreover, the resistive part ($R_L$+$R_C$) was much higher (17 Ω) in the bare MWCNT sample than in the sputtered sample (5.1 Ω) (Table 2).

**Table 2. The fitting parameters obtained for the components in the equivalent circuit. In the case of the reference SMD resistor, the circuit is simplified to a series $R_L$ and $L$ (i.e. $R_C$=0 Ω and $C$=0 F) (Paper III).**

| | $R_L$ (Ω) | $R_C$ (Ω) | L (H) | C (F) |
|---|---|---|---|---|
| Reference SMD resistor | 1.1482 | – | 5.68e-10 ± 2.156e-12 | – |
| Bare MWCNT film | 11.09 ± 0.003 | 7.04 ± 0.039 | 2.13e-9 ± 9.878e-10 | 2.7e-11 ± 8.011e.12 |
| Cu/Cr sputtered MWCNT film | 1.14 ± 0.001 | 3.99 ± 0.0136 | 4.75e-10 ± 9.256e-12 | 1.21e-10 ± 8.484e-12 |

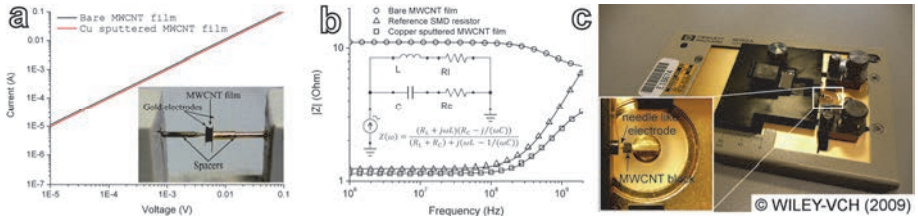


**Fig. 13. a) The measured *I-V* curves of MWCNT films (thickness of 1.0 mm, footprint area of 1.5×1.5 mm$^2$) fixed between slightly pressed gold contact electrodes. b) Results of impedance measurements up to 1 GHz for reference SMD resistor (triangle), CNT film sputtered with Cr/Cu contacts (square) and bare CNT films (circle). Inset shows the equivalent circuit model of the MWCNT films. c) The Hewlett-Packard 16192A test fixture. Inset shows the contact electrodes of the test fixture (Paper III, published by permission of WILEY-VCH).**

### *4.2.2 Sliding electrical contact brushes*

To demonstrate the feasibility of sliding CNT brush contacts, the MWCNT forests were mounted on flexible brass cantilevers to form brush-type structures. These were brought into contact with the slightly modified commutator of the electric motor (Johnson Electric, 6 500 rpm at 12V). The optimal pre-pressing force (72mN) was set for both brushes with 2 translation stages controlled with micrometres precision (Figure 14).

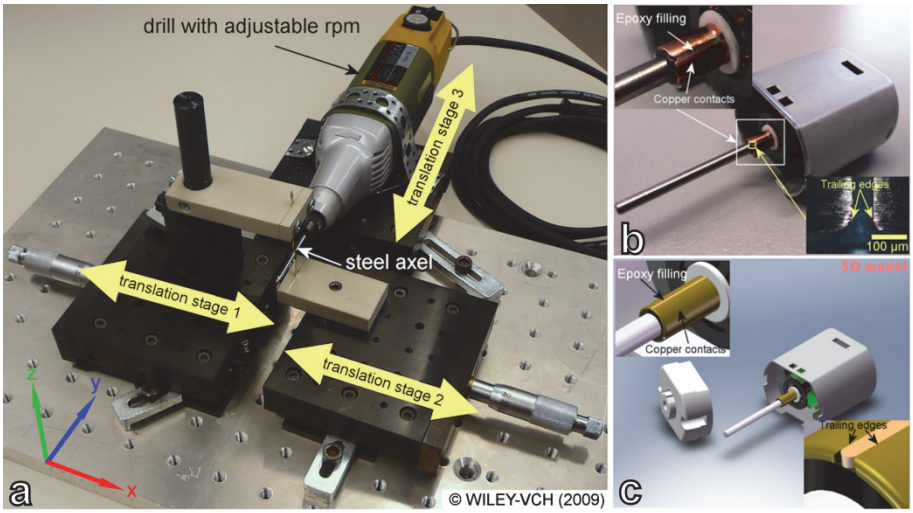


**Fig. 14. a) The experimental setup used consisting of three translation stages for precise pre-pressing force adjustments. "Translation stage 3" accommodated the electric motors and the adjustable rpm drill (shown here). The two perpendicular stages were for setting the pre-stress values. They consisted of a holder which allowed the switching of brass cantilevers and commercial brush or MWCNT brush on brass cantilevers for electric contacts. b) And c) Images and computer graphics of the reduced trailing edges, respectively. The gaps in the commutator were filled with epoxy in order to obtain as smooth a surface as possible (Paper III, published by permission of WILEY-VCH).**

The measurements were carried out under constant current conditions (14 mA, with 12 V compliance voltage limit). The MWCNT brush contacts resulted in steadier and more regular voltage values with significantly less noise than with the ordinary carbon–copper composite brushes. The smaller level of fluctuation in the voltage was most likely due to the smooth sliding of the soft nanotube film on the irregular rotating surface, as the films conformed to the non-uniform roughness of the surface. The voltage drops and sharp peaks in the time series graphs (Figure 15a–b) derived from the trailing edges of the commutator bar. Both types of brushes exhibited higher bulk stiffness in comparison to the cantilever spring that dominated the macroscopic normal forces (smooth rounded shape in Figure 15a–b). However, clear differences for the brushes were seen for the tangential stiffness where the cantilevers and solid brushes were stiff but the CNT brush was soft. Mechanical chopping by bar edges caused significant

bouncing and noise for the solid brush while the CNT brush conformed to the irregularities and changes in friction forces by shear deformation.

Using a pre-stress force of 72mN, the same current was maintained by similar voltages (~3.5 V, corresponding graphs are highlighted with grey colour in Figure 15) for the two setups. A drastic increase of instability was observed when excessive pressing force (98 mN) was used, especially in the case of the nanotube brushes as a consequence of intimate interaction with the commutator surface and severe bouncing at the interfaces. On the other hand, the contact resistance was decreased but the performance of both types of brushes still became unsatisfactory. In contrast to the higher pressing forces, a lower pressing force (48 mN) resulted in a double frequency signal (Figure 15a) as the brush had more freedom to run off the surface, creating continuous bouncing and intermittent contacts with the commutator. Moreover, the contact resistance was increased and the change in contact resistance was more pronounced in the nanotube sample.

Even though the experiment lasted typically several hours and in one case lasted up to five days, the MWCNT brushes were fully operational throughout. After one million motor revolutions (~2.5 hours of usage), some minor wear appeared on the surface. This was a result of milling up and re-alignment of the top-most region of the nanotube block caused by the edges of the rotating commutator. However, no fracture, detachment or any other structural damage was observed. This could be explained by the mechanical robustness and good thermal conductivity of the nanotubes. Moreover, the local buckling and crinkling observed in repeated contact cycles seemed to disappear by self-healing, as had been previously observed by Cao *et al.* (2005).

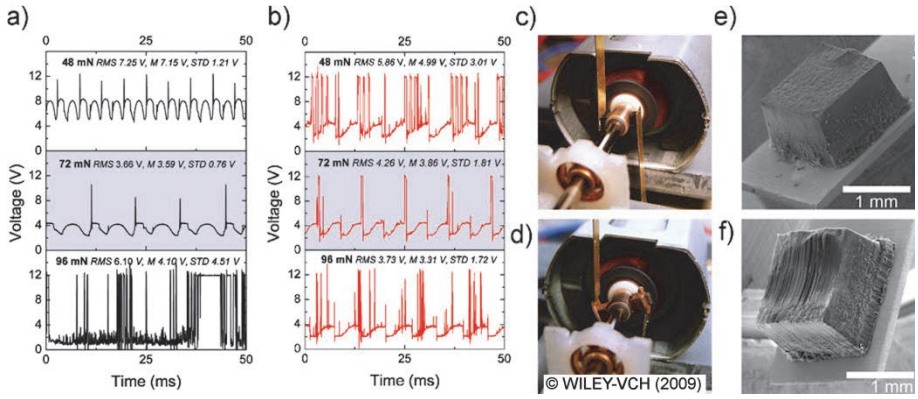


**Fig. 15. MWCNT and conventional contact brushes applied in electric motors. Voltage fluctuation measured during normal operation when a constant current was maintained for a) MWCNT and b) commercial graphite–copper composite brushes. The curves correspond to the measurement results taken when 48, 72, and 96mN force were applied from the top to the bottom, respectively. Photographs of the experimental arrangements of the MWCNT (c) and conventional brush (d) setups. FESEM image of the CNT brush–on–brass cantilever assembly (e) and the wear after several hours of operation (f) (Paper III, published by permission of WILEY-VCH).**

In order to obtain relevant data on electrical noise levels from the contact brushes, the brushes were brought into contact with the rotating highly polished stainless steel axle (typical surface roughness of < 1 μm) of the electric motor (Johnson Electric, ~3600 rpm at 12 V) (Figure 16). A constant driving current of 10 mA was applied through the brush–axle–brush contacts and the voltage drop over the contacts was measured with an oscilloscope. A high pre-stress force (144mN) was applied to achieve a low contact resistance. The nanotube contacts showed almost an order of magnitude lower contact resistance (corresponding graphs are highlighted with grey colour in Figure 16a–b) and a two orders of magnitude lower noise intensity compared to the monolithic brush used in the experiments (Figure 16c). In general, the power density spectra showed similar frequency characteristics for both brushes derived from the similar fixture and spring constant of the cantilevers. Therefore the resonances of both brush setups were similar. However, slightly lower bending-resonance frequencies were detected for the commercial carbon–copper composite brush because of the greater density (~2.84 $g \cdot cm^{-3}$) and mass compared to the MWCNT brush (~0.3 $g \cdot cm^{-3}$) (Paper III).

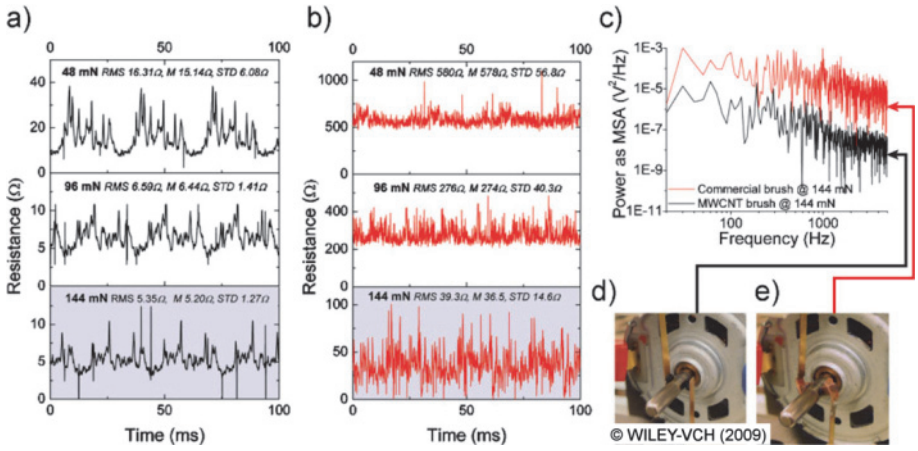


**Fig. 16. Electrical signal fluctuations measured on rotating axles contacted by MWCNT and conventional brushes. Resistance fluctuation measured on MWCNT and commercial brushes setups are presented in a) and b), respectively. In c) the power density spectra indicate the superior noise characteristics of nanotube brush contacts in comparison with solid carbon–copper composite brushes. Photographs of the experimental arrangements with carbon nanotube and conventional brushes are shown in d) and e), respectively (Paper III, published by permission of WILEY-VCH).**

### *4.2.3 Rotating electrical contacts*

In analogy to the sliding nanotube brushes, another type of rotating contact can be made from aligned nanotube films where the nanotubes are grown on cylindrical objects. Possible applications for such contacts are unipolar generators, motors, and a wide variety of electromagnetic launchers that require high current density electrical contacts sliding over a smooth counter surface.

To demonstrate such contacts; which must exhibit low noise and small contact resistance, nanotube films with a thickness of ~1.0 mm were grown on quartz rods (length of 40 mm and diameter of 2 mm, Goodfellow). The rods with CCVD grown nanotube forests were then contacted with flexible brass cantilevers in a similar fashion to the earlier experiments (Figure 17g). For comparison, an ordinary smooth stainless steel axle was contacted by brass cantilevers in a similar way. After a few minutes of operation, some visible wear in the location of the contact appeared on the nanotube axle as the brass cantilever slightly

compressed the nanotube film resulting in a ~100 μm deep trench (Figure 17f). This change in the geometry did not, however, result in any operational failure.

As shown in Figure 17c, the contacts between the cantilevers and the rotating nanotube film showed linear *I–V* behaviour, as expected from the previous experiments. To demonstrate the low noise operation, a constant current source (10 mA) was applied through the brush–axle–brush contacts while measuring the voltage drop over the setup (brush–axle–brush) with an oscilloscope. By applying a relatively small pre-stress force (48 mN), the nanotube contacts exhibited a slightly lower contact resistance (corresponding graphs are highlighted with grey colour on Figure 17a–b) and significantly less electrical noise compared to the brass–steel–brass contact (Figure 17d). At higher frequencies the carbon nanotube contact was less noisy because its power spectrum was close to a $1/f^2$ shaped response in the frequency region of > 100 Hz. At the same time the power spectrum for the steel axle setup was closer to white noise (i.e. a random signal with an almost flat power spectral density). The dissimilarity of the noise spectra demonstrated the advantageous damping properties of the MWCNT film, as well as the good electrical contact provided by a compressed spring-like nanotube contact.

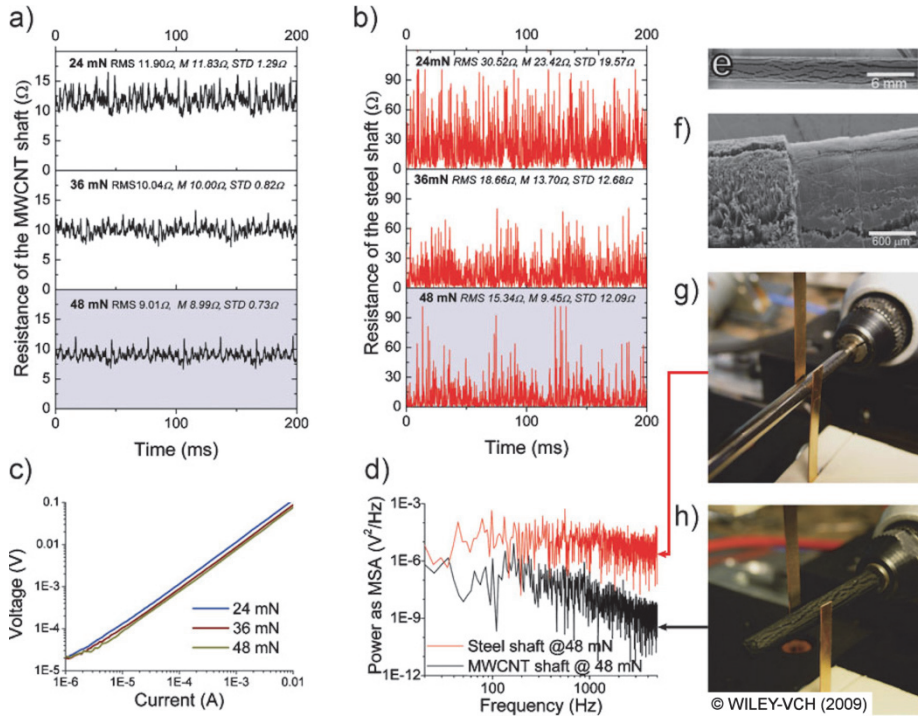


**Fig. 17. Electric contact measurements performed with rotating MWCNTs. a) And b) show resistance fluctuation for MWCNT and steel axles measured under constant current conditions and with different pre-stress forces, respectively. c) *I–V* characteristics of the rotating MWCNT axle at different pressing forces. d) Power density spectra calculated from (a) and (b). e) And f) show the as-grown MWCNT film on a quartz rod and the shallow trench after usage, respectively. Photographs of the experimental arrangements performed with a steel axle and carbon-nanotube-coated quartz axle are shown in g) and h), respectively (Paper III, published by permission of WILEY-VCH).**

### *4.2.4 Hot switching application with MWCNT brush contacts*

The MWCNT films were examined in hot switching experiments with a gold pin contact to establish the stability of the electrical contact during repeated cyclic contact events. There is a similarity between the sliding electrical contact and repeated contact applications, such as switches. The motivation for using nanotubes as switching material in this type of contact application was that it was

believed that the MWCNT local contacts are elastic and are distributed across the footprint of the contact. This is in contrast to the traditional brush and switch materials in which the high elastic modulus and the light loads used cause the real area of contact in practice to be many orders of magnitude lower than the apparent area. Therefore, the super-compressibility and current-carrying properties of MWCNTs could provide a unique solution giving pressed elastic contacts and high interfacial contact area with good electrical conductivity even at light loads.

The schematic of the experimental setup is shown in Figure 18a. The vertically aligned MWCNT block was fixed in place while a gold coated glass lens was moved with a piezo-driven actuator (in on-state the peak-load was 500 μN) to demonstrate the on–off switching. The robustness of these nanotube blocks and the stability of the electrical contact resistance were demonstrated by a prolonged hot-switching experiment (Figure 18b) where the switching was repeated up to 100000 times (over 4 days of operation). The nanotube block maintained its properties in that no mechanical wear or increase in contact resistance (< 1 Ω after 100000 cycles) was observed during that time.

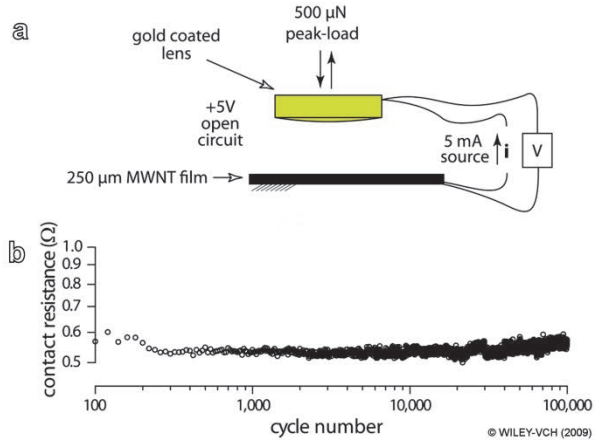


**Fig. 18. Reliability test with a point contact setup. a) The schematic of the experimental setup showing the 4–point probe measurement and arrangement of the voltage and current source. b) Contact resistance over 100 000 cycles is shown to be below 1 ohm and steady for the entire experiment, which was run in open air over 4 days (Paper III, published by permission of WILEY-VCH).**

# 5 Thermal management applications with carbon nanotubes

Short individual carbon nanotubes have been shown to exhibit excellent thermal conductance, which is due to ballistic phonon transport. However, the use of individual nanotubes is impractical in most cases. Forests of aligned nanotubes are thought to be potential candidates in thermal management applications, e.g. in miniaturized cooling fin structures for direct heat dissipation, hot-spot removal and also as thermal interface material. Here the thermal properties (thermal diffusivity and conductivity) of freestanding CCVD grown MWCNT forests are studied and the fin-structured nanotube forests are used as effective cooling elements (heat sinks) on alumina chips.

## 5.1 Background

Though thermal conductivity of short nanotubes is excellent because of the ballistic phonon transport, in the case of long nanotubes, bundles and thick forests, diffuse transport tends to dominate due to phonon scattering on defects. Thus the corresponding thermal diffusivity and conductivity values are significantly inferior to those of short individual nanotubes (Yi *et al.* 1999) but are still good enough to compete with metals and ceramic materials. In addition, CNTs have several other excellent properties such as light weight, large specific surface area, excellent mechanical strength, high aspect ratio, flexibility and anisotropic thermal diffusivity/conductivity (Borca-Tasciuc *et al.* 2005, Ivanov *et al.* 2006) making them ideal candidates for thermal management applications in electrical components and devices (Kordás *et al.* 2007, Fu *et al.* 2012) as well as in polymer composites (Ni *et al.* 2012). However, direct applications of CNTs in electronics are often limited by the high synthesis temperature (Takagi *et al.* 2006) and poor adhesion to their growth substrate (Dai 2002). During the past years, various printing techniques and soldering based transfer methods have been proposed to overcome these difficulties (Kordás *et al.* 2006, Fu *et al.* 2010).

## 5.2 Thermal properties of MWCNT forests

MWCNTs were grown on $Si/SiO_2$ chips (200 nm thermal $SiO_2$) as round structures (diameter of 1.27 cm) using the CCVD method (Halonen *et al.* 2008). The sample shape and diameter/size was defined by the sample holder geometry

of the measurement device used. Ferrocene/xylene precursor (0.02 $g \cdot mL^{-1}$) with 0.1 $mL \cdot min^{-1}$ feeding rate was evaporated at ~190 °C before introducing it to the heated (770 °C) horizontal reactor with Ar carrier gas (flow of 40 $mL \cdot min^{-1}$). The growth time was adjusted to achieve appropriate CNT forest thicknesses.

To obtain freestanding films, the grown CNT samples were placed in a closed box with an open crucible filled with HF (48% vol.) and left there overnight. The fumes of the hydrofluoric acid react with the $SiO_2$ surface forming volatile fluoride complexes leading to an etching of the uppermost oxide layer and thus detaching the nanotube forest from the surface. The forest can then easily be removed using a sharp/thin object. Although this method was found to be effective for thicker samples (CNT forest height > 1 mm), detaching thinner samples (height < 1 mm) was more challenging due to the high film porosities. Because amorphous carbon content is also formed on the samples during the CCVD growth process, two types of samples were prepared: as grown samples, and samples annealed in an open-air furnace at 400 °C for 2 hours. The purpose of annealing was to burn off the amorphous carbon content thus purifying the films. TEM and FESEM analyses were performed on both types of sample (Figure 19).

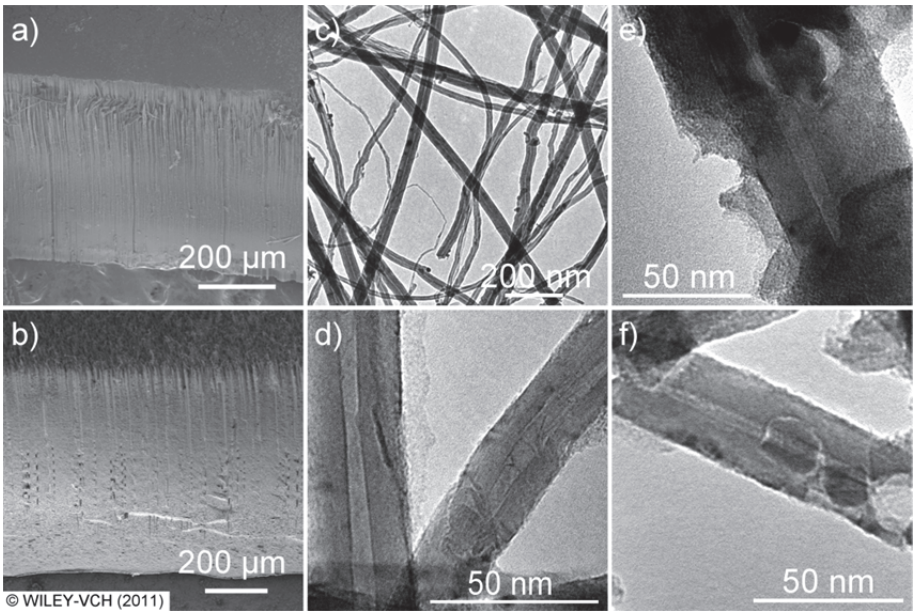


**Fig. 19. (a) And (b) FESEM images taken from the sides of the 1.5 mm and 1.9 mm thick MWCNT samples, respectively. c) And (d) TEM images of carbon nanotube samples from as-grown sample. (e) and (f) TEM images taken after annealing in air (Paper IV, published by permission of WILEY-VCH).**

The forest height was evaluated from FESEM images, while the diameter distribution was assessed from TEM images by analyzing more than 100 different nanotubes. The FESEM analysis showed a good alignment of nanotubes in the samples (Figure 19a–b). According to the TEM analysis, the nanotubes were quite straight suggesting only a small defect density in their walls; however some parts of the tubes were coated with amorphous carbon (Figure 19c–d). After the annealing process, formation of defects and cracks in the walls was more clearly observed (Figure 19e–f). The nanotubes had diameters between 15 and 90 nm as assessed by TEM. The nanotube diameter was increased in thicker CNT forests due to the longer growth time.

The baseline corrected Raman D– and G–band peak positions, together with the corresponding intensity ($I_D/I_G$) ratios, are presented in Table 3 and Figure 20. Since the density of the films was decreased to ~70% of the original value due to the partial burning off of the amorphous carbon, we should expect a more pronounced decrease of the $I_D/I_G$ ratio. However, the fairly constant value

suggests that the formation of defects in the graphitic lattice caused by the annealing process was considerable. This was observed in the TEM analysis as explained earlier.

**Table 3. D– and G–band peak positions and intensity ratios ($I_D/I_G$) of MWCNT samples (Paper IV).**

| | MWCNT 1.5 mm | | MWCNT 1.9 mm | |
|---|---|---|---|---|
| | as-grown | annealed | as-grown | annealed |
| D band peak ($cm^{-1}$) | 1366.4 | 1362.0 | 1364.2 | 1362.0 |
| G band peak ($cm^{-1}$) | 1586.2 | 1584.1 | 1590.5 | 1586.2 |
| $I_D/I_G$ ratio | 0.46 | 0.46 | 0.62 | 0.55 |

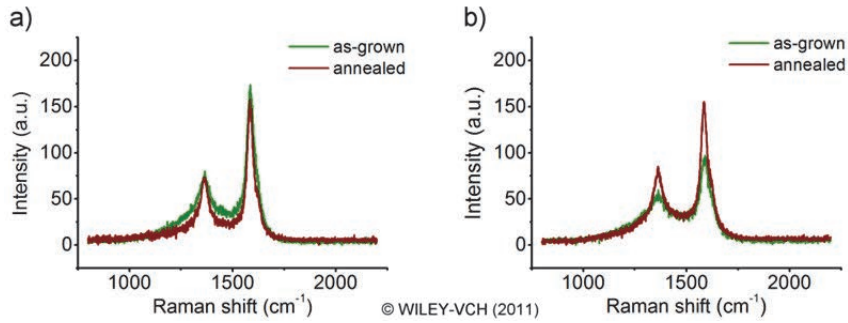


**Fig. 20. Raman spectra measured for (a) 1.5 mm and (b) 1.9 mm thick MWCNT samples before and after annealing in air (Paper IV, published by permission of Wiley-VCH).**

### *5.2.1 Characterization of thermal properties*

The temperature dependent thermal diffusivity of freestanding CCVD grown MWCNT forests was measured using a flash method with a Flashline 3000 thermal properties analyzer (Anter corp.) in the temperature range of 25 °C to 200 °C. This device uses a high speed xenon (Xe) discharge (HSXD) pulse source to create a short intensive heating pulse which heats the sample surface rapidly. From the rise time of the rear face thermogram (measured with a liquid nitrogen cooled indium detector) the thermal diffusivity (α) can be calculated by:

$$\alpha = 0.1388 \times L^2 \times t_{50\%}^{-1} \quad (5)$$

, where $L$ is the sample thickness and $t_{50\%}$ is the time for the rear face to reach 50% of the maximum temperature value (Parker *et al.* 1961). The principle of the flash

method together with the measurement device used is presented in Figure 21. Ideally (Figure 21b) the rear face temperature remains at its maximum value but in reality the temperature decreases slightly with time due to radiated heat losses. The dimensions of the sample holder (Figure 21d) determined the sample size and consequently short free-standing nanotube films were found to be unsuitable for this measurement.

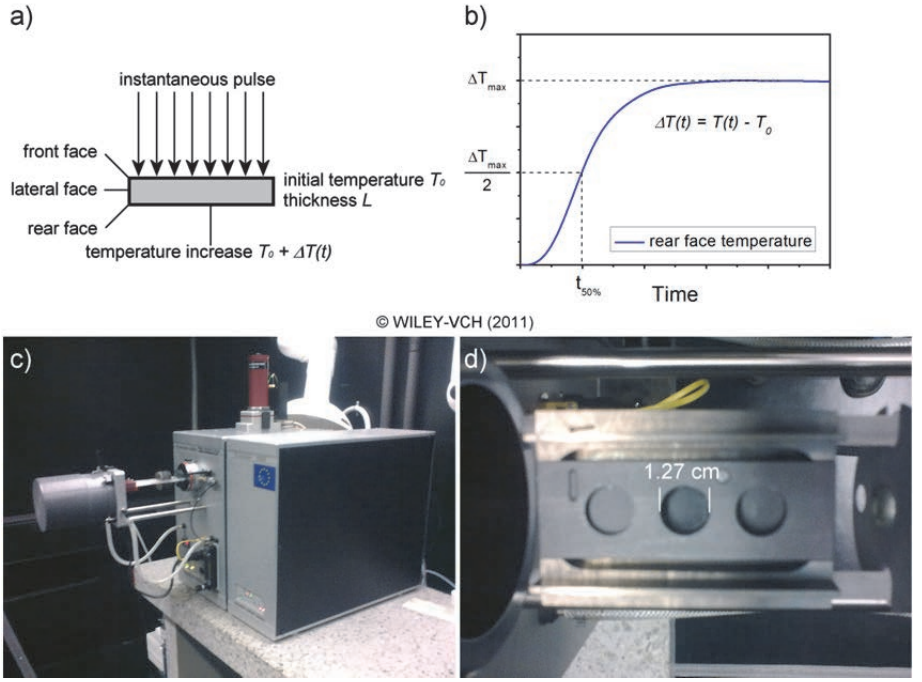


**Fig. 21. The basic measurement principle of the flash method (a) and an ideal thermogram (without heat losses) obtained at the rear face of the specimen (b) (Paper IV, published by permission of WILEY-VCH). (c) Flashline 3000 thermal properties analyzer (Anter corp.) and (d) the sample holder of device.**

To validate the experimental setup and measurement data, metal blocks made of copper and an aluminium alloy were used as reference samples. These were chosen for their well-known thermal properties. To ensure black body conditions similar to that of the nanotube samples, both rear and front faces of these metal blocks were spray coated with graphite (Figure 22).

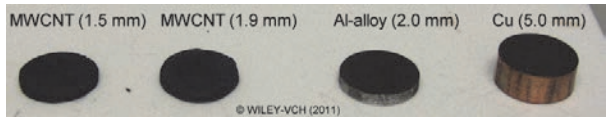


**Fig. 22. Photograph of MWCNT (1.5 mm and 1.9 mm), Al–alloy (2.0 mm) and Cu (5.0 mm) disks used in the measurements. Note: the front and rear faces of the metal disks are coated with graphite (Paper IV, published by permission of WILEY-VCH).**

The measured thermal diffusivities for the reference Cu and Al-alloy samples were in good agreement with values in the literature (Holman 2002). In addition, the results showed the expected slight decrease in thermal diffusivity with increasing temperature. The as-grown MWCNT samples exhibited almost identical thermal diffusivity between each other, being about 0.45 $cm^2 \cdot s^{-1}$ at room temperature and showed a similar decrease of diffusivity with increasing temperature. However, the annealing process caused the thermal diffusivity to decrease to about half of the original value, being 0.22–0.25 $cm^2 \cdot s^{-1}$ (Figure 23).

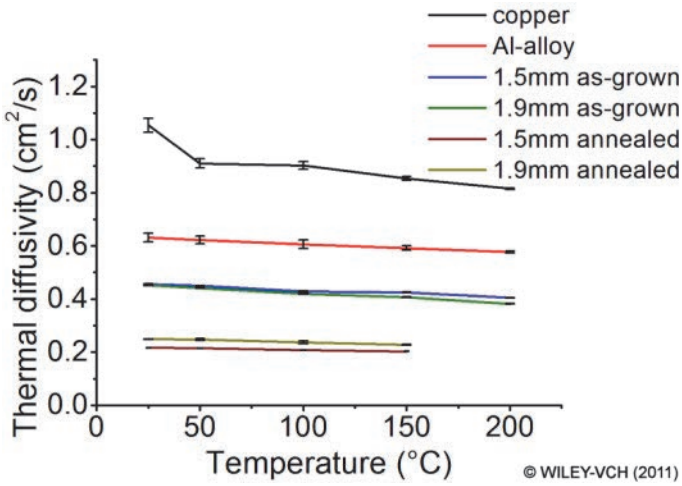


**Fig. 23. Measured thermal diffusivities plotted as a function of temperature in the temperature range of 25–200 °C. NOTE: The plots are averages of three individual measurements (Paper IV, published by permission of WILEY-VCH).**

The density of the MWCNT samples decreased about 30% together with the thermal diffusivity, i.e. heat treatment is clearly increased the already high film porosities even further. The high porosity of the samples also meant that the

average distance between the nanotubes was rather large. These decreased mass densities resulted in reduced thermal diffusivity values for the annealed samples. Moreover, in the light of the TEM and Raman analyses, the reduced diffusivity is not very surprising on the defected lattice. As a whole, the decreased thermal diffusivity of the annealed samples was due to both reduced mass densities and a more defective lattice caused by the annealing process.

### *5.2.2 Thermal conductivity of freestanding MWCNT forests*

The thermal conductivity, $k$, of all measured materials was calculated from the specific heat, $c$, density, $\rho$, and measured thermal diffusivity, $\alpha$, by:

$$k = c \cdot \rho \cdot \alpha \tag{6}$$

In the calculations, the values for specific heats of materials were taken from the literature and the densities of MWCNT films were determined by measuring the dimensions (height and diameter) and weighing the samples. The calculated data is summarized in Table 4.

**Table 4. Thermal conductivities calculated from measured thermal diffusivities and densities for reference samples and MWCNT samples at room temperature (25 °C) (Paper IV).**

| | C ($J \cdot kg^{-1} \cdot K^{-1}$) | α ($cm^2 \cdot s^{-1}$) | ρ ($kg \cdot m^{-3}$) | $k$ ($W \cdot m^{-1} \cdot K^{-1}$) |
|---|---|---|---|---|
| copper | 385[a] | 1.05 | 8920 | 361 |
| Al-alloy | 897[a] | 0.63 | 2680 | 152 |
| MWCNT 1.5 mm | 704[b] | 0.46 | 313 | 10 (as-grown) |
| MWCNT 1.5 mm | 704[b] | 0.22 | 221 | 3.4 (annealed) |
| MWCNT 1.9 mm | 704[b] | 0.45 | 263 | 8.4 (as-grown) |
| MWCNT 1.9 mm | 704[b] | 0.25 | 187 | 3.3 (annealed) |

[a] Holman (2002), [b] Huang *et al.* (2011)

Considering the mass density of individual nanotubes (~2200 $kg \cdot m^{-3}$) (Li *et al.* 2007), the density of as-grown films (~300 $kg \cdot m^{-3}$) and their calculated thermal conductivities from the measured diffusivity data of the as-grown MWCNT films (10 $W \cdot m^{-1} \cdot K^{-1}$), the thermal conductivity of individual CNTs in the forest was estimated to be about 70 $W \cdot m^{-1} \cdot K^{-1}$. The slightly lower thermal conductivity for 1.9 mm thick as-grown MWCNT sample could be explained by the more defective lattice. Also the density comparison showed higher porosity for the thicker sample, which resulted in a lower thermal conductivity. Similar to the

thermal diffusivity results, the effective thermal conductivity was also decreased after thermal treatment.

Based on the measured results, it can be concluded that in the right conditions MWCNT films can outperform ordinary thermal interface materials and may be alternatives for Al and Cu components in thermal management (heat removal/dissipation) applications. Further improvements are expected to be achieved by using shorter nanotube forests having lower defect concentrations and higher film density.

## 5.3 Chip cooling application with MWCNT forests

To exploit the measured thermal properties of MWCNT forests in a real application, carbon nanotubes were utilized in a chip cooling application as an effective heat sink material. The test chips were fabricated as follows:

1. CCVD growth of MWCNT pillar structures.
2. Laser scribing of 2 inch alumina template into desired size (6.0×8.0 $mm^2$) and laser drilling of holes into chips for electrical contacts and suspended cooling performance measurements.
3. Thick-film screen printing of heater structure and solder pads (following consequent drying + firing). A total of 12 chips were fabricated together on a 2 inch square alumina template.
4. Sputtering the CCVD grown MWCNT films (fin structure) with Cr (15 nm) and Au (450 nm).
5. Stencil printing of solder paste on solder pads.
6. Placing the CNTs with a fine placer (Finetech bonding force applicator) on soldered electrodes.
7. Soldering the CNT films in the hot plate of the fine placer.
8. Detaching the Si substrate from the CNTs with HF fume.

CNTs were grown using the previously described CCVD method on pre-patterned $Si/SiO_2$ substrates. The synthesis time was adjusted to obtain CNT pillars with a height of ~800 μm. The nanotubes were characterized with TEM, FESEM and Raman spectroscopy. The CNTs exhibited quite a narrow diameter distribution (10–70 nm, average diameter of 25 nm). Moreover, they were rather straight, suggesting only a small defect density in their walls. The low ratio of D–band and G–band peak intensities obtained from Raman spectroscopy analysis (Horiba

Jobin-Yvon Labram HR-800 Raman microscope, λ=488 nm) also indicated a good graphitization and alignment of the nanotubes (Figure 24).

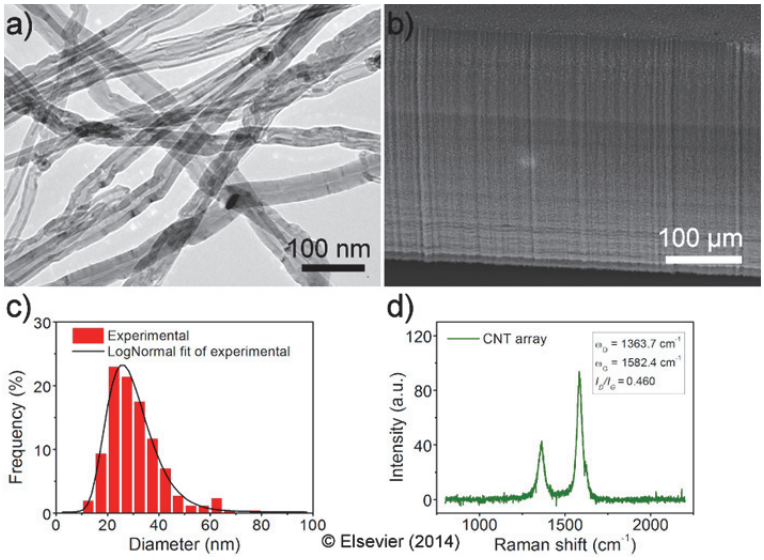


**Fig. 24. (a) Transmission electron micrograph, (b) scanning electron microscopy image taken from the side of the CNT structure, (c) diameter distribution, and (d) a typical Raman spectrum of the grown multi-walled CNTs used in the experiments (Paper V, published by permission of Elsevier).**

Polycrystalline alumina substrates (thickness 250 µm) were laser scribed into 6.0×8.0 $mm^2$ size chips and holes (~300 µm in diameter) for wire connections were drilled with the same laser (Siemens Microbeam 3200). The heater structure and solder pad (3.0×3.0 $mm^2$) were screen-printed (Speedline Microflex) on the chips using a platinum paste (DuPont 9141) and a silver paste (DuPont 6160), respectively. Platinum wires of 250 µm diameter were used as electrical contacts and also as mechanical support for the test chips during the subsequent cooling performance measurements (Figure 25).

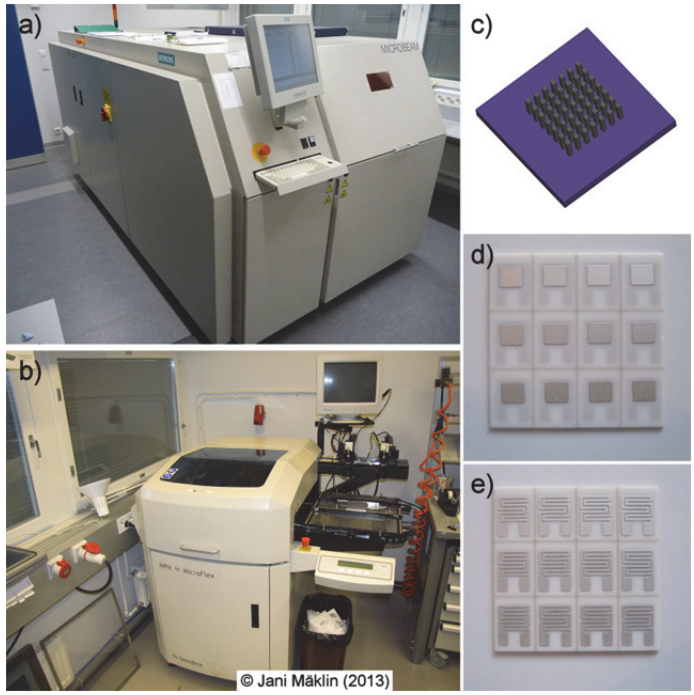


**Fig. 25. Equipment used in test chip fabrication. The laser and screen-printer are shown in (a) and (b), respectively. (c) The CNT growth template with CNTs (d) and (e) Top and bottom sides of 2 inch alumina template with printed and sintered structures, respectively.**

Computational fluid dynamics (CFD) simulations were performed to optimize the finned cooler structure. For the purpose of the simulations, a 3×3 $mm^2$ sized heat sink with variable heat sink fin number (4–10) and fin thickness (100–400 µm) was assumed with a heating power of 500 mW. However, a cooler structure with a 7×7–array of 250×250 $\mu m^2$ fins with 200 µm spacing was found to be one of the best structures for optimal heat dissipation under measurement conditions.

### *5.3.1 Solder transfer of MWCNT structures*

In order to facilitate the successful transfer of the CNT films to the Ag solder pads of the ceramic chips, thin films of Cr/Au (30 nm/450 nm) were sputtered on the nanotubes after growth. This treatment ensured an intimate contact, improved interaction on the interface (thermal interface between the pad and nanotubes),

and also provided a surface with the proper wetting properties that are important in soldering. The schematic of the transfer method, together with FESEM and optical images of grown and transferred CNT arrays, are shown in Figure 26.

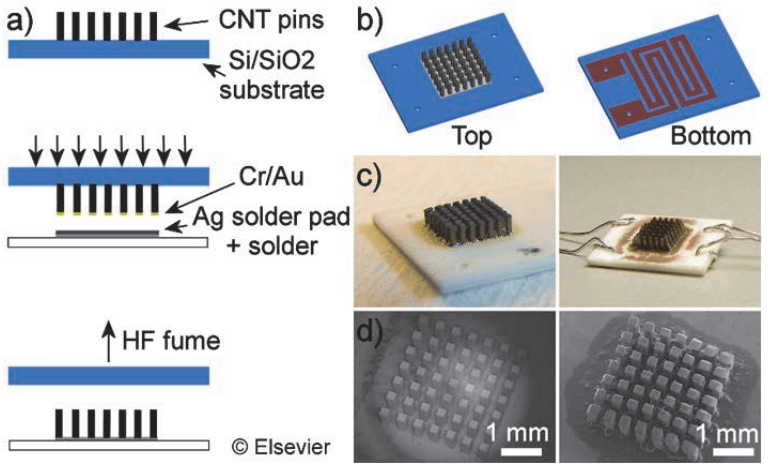


**Fig. 26. Schemes of (a) CNT film transfer and (b) the two sides of a ceramic test chip. (c) Optical images taken from a nanotube cooler and laser-structured copper cooler mounted on a ceramic chip. (d) Scanning electron microscopy images taken from the fin structures before (left) and after soldering (right), (Paper V, published by permission of Elsevier).**

The transfer of the nanotubes from the growth templates to the ceramic chips was carried out with a placing tool (Finetech 145) equipped with a hot plate, manipulators and a video camera for online monitoring of the process (Figure 27). A thin layer (~150 µm) of solder paste (Qualitek DSP 618D, Sn–Ag–Cu alloy, melting point 220 °C) having high thermal conductivity (58.7 $W \cdot m^{-1} \cdot K^{-1}$) was stencil printed on the solder pad of the ceramic chip and the chip was placed on the hot plate of the fine placer. Principally, any foot-print sized films could be transferred to the solder pads using this method. The transfer method was found to be suitable for transferring the CNT pins with a reasonably high yield (> 90 %) without damaging the original structure.

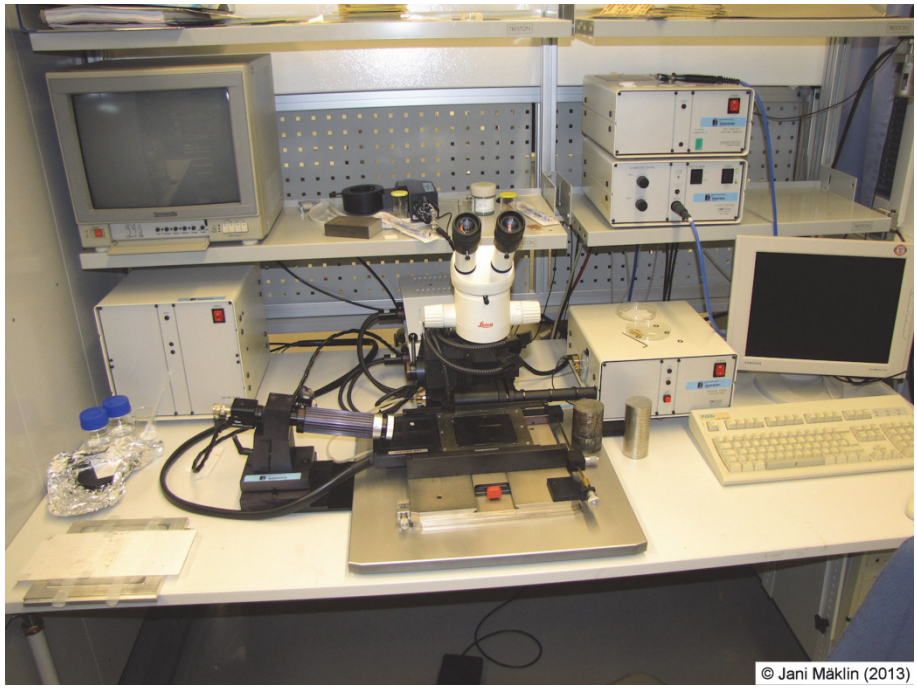


**Fig. 27. The soldering station used for transferring the CNT structures onto ceramic chips.**

In the course of soldering, the temperature of the hot plate was increased to 240 °C with a heating rate of 50 °C·min$^{-1}$, kept there for 1 min and then cooled down to 50 °C while continuously pressing the cooling fins onto the ceramic chip. Continuous pressing was important to ensure the solder joint had as low a thickness as possible and to avoid any air pocket that would limit heat transfer from the chip to the nanotubes (Figure 28). After soldering, the substrate of the nanotubes was exposed to the vapour of aqueous HF:EtOH (1:4) solution to separate the CNT structure from the growth template.

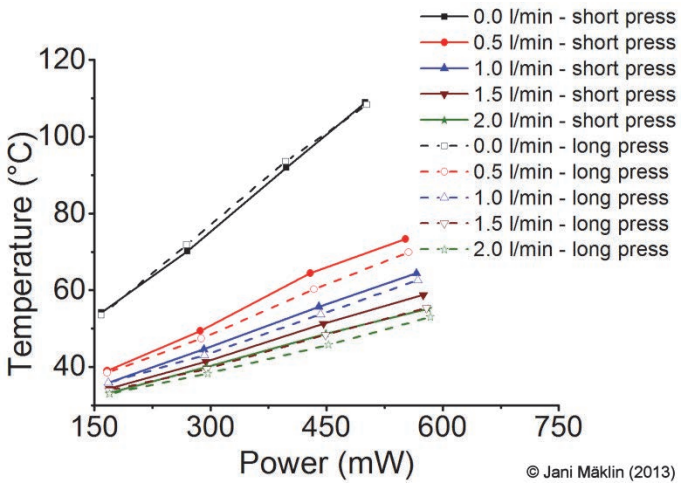


**Fig. 28. A comparison cooling performance measurement performed with similar copper coolers on test chips using different pressing times during the soldering process.**

### *5.3.2 Mechanical testing of soldered CNT pillars*

In order to validate a good adhesion between the CNT pillars and the target substrate, an adhesion test was performed using a load-cell sensor (Kyowa LTS-50GA). In each measurement, an individual pillar of the soldered nanotube pattern was attached to the tip of the probe by dipping the probe tip of the load cell in cyanoacrylate and then introducing the probe tip into contact with a single soldered CNT pillar. After the adhesive was dried, the load cell was lifted up with a custom-made stage at a constant speed until the pillar detached from the target substrate. The force was continuously monitored during the lifting of the load cell. The adhesion force was found to be about 70 mN. The corresponding strength (stress) could be calculated from the force by dividing it with the attaching area of the pillar ($250\times10^{-6}\times250\times10^{-6}$ m$^2$). The obtained stress was $1.12\times10^6$ Pa (Figure 29). It is worth noting that this value is very close to the value ($1.08\times10^6$ Pa) measured by Fu *et al.* (2008), even though they used a different soldering process and measurement method in their experiments. As seen in Figure 29, the measured force started to increase linearly when the load-cell was lifted up. This confirms that the lifting was applied in the axial direction only. At the point where the nanotube pillar detached from the substrate the measured force decreased

instantaneously. The subsequent oscillation was a consequence of the detaching of the nanotube pillar.

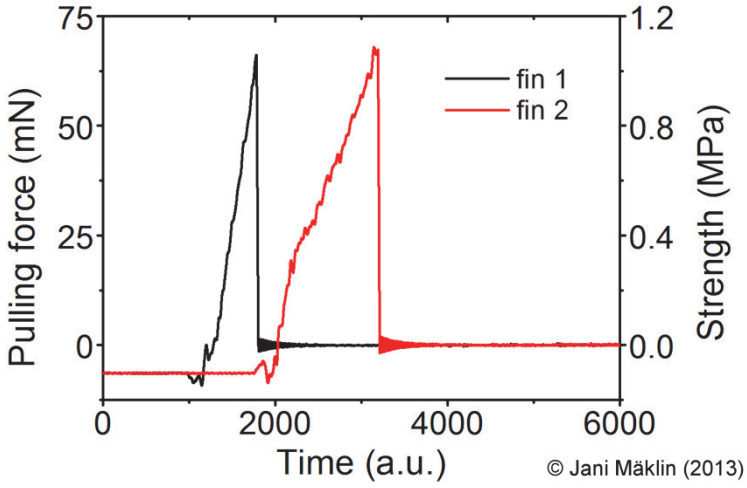


**Fig. 29. Adhesion tests performed for soldered CNT pillars.**

### *5.3.3 Cooling performance of nanotube coolers*

In order to have a valid reference cooling structure, a copper plate of thickness of 800 µm was laser-structured into geometry similar to that of the CNT coolers and mounted on ceramic chips using the same transfer method. Before making any measurements, the temperature coefficient of resistance of the heater was evaluated to be 0.00322±0.00006 $°C^{-1}$. This was based on averaged 4–point measurement data from 12 devices measured in the temperature range between 25 °C and 220 °C.

In the cooling efficiency experiments, a current was driven through the heater while measuring the voltage in order to calculate the dissipated power. The chip temperature (derived from the Pt heater resistance) versus heating power was recorded under various thermal loads. The heating powers used were in the range of 150 mW to 500 mW, which corresponded to temperatures between 50 and 120 °C. The electrical measurements were carried out in 4–point probe setup (Keithley Instruments dual channel SourceMeter, model 2636). During measurement the chips were suspended on Pt wires that were connected to the printed heaters. Forced air flow was blown perpendicularly from the top of the

sample through a 1 mm diameter nozzle from a distance of 8 mm with flow rates of 0.0–2.0 $L \cdot min^{-1}$. Moreover, a thermal camera (Flir b60) was used to obtain thermal images of the chip under test. The thermal camera images (Figure 30a) show the cooling effect of the nanotube cooler structure. The coolest spots, i.e. those visible at the perimeter of the pad structure, corresponded to the positions of the pillars of the CNTs, showing that the temperature around the tip of the pins was lower than that of the chip's surface. A rectangular shaped cooler area inside the hot pad was visible under forced cooling gas flow because of the impingement of the cooling gas inside the cooler structure. Moreover, this area related to the geometry of the pillar structure of the CNT cooler (7×7 rectangular array). However, the optical resolution of the thermal camera (350 µm/pix) was not sufficient to show the entire cooler geometry. The chip temperature versus heating power plots (Figure 30b) show that the cooling performance of the CNT-based cooler was comparable to that of the copper within the studied flow and heating power ranges. The nanotube based coolers showed only minor advantages over copper; however the differences were close to the error margins of the electrical measurements.

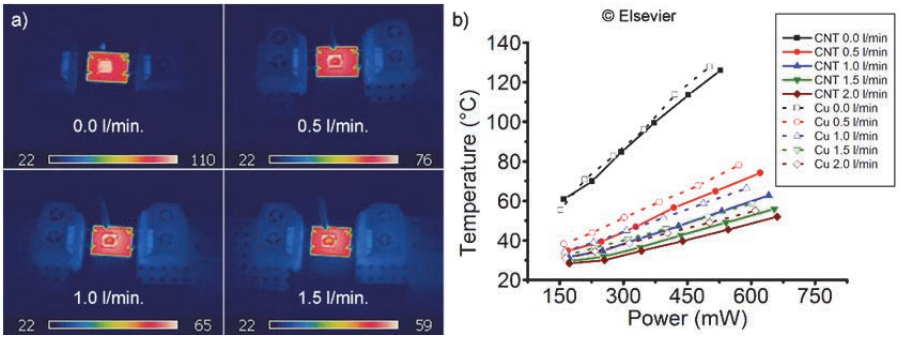


**Fig. 30. (a) Thermal camera images taken from a test chip under test. Note: the cooler structure cannot be seen on the thermographs due to the low resolution of the camera (optical resolution ~350 µm/pix). (b) Cooling performances of CNT- and Cu based coolers of similar geometry. Note: the graph shows the average performances of three different coolers of both types. The error margins in the measurements are ±2 % (Paper V, published by permission of Elsevier).**

To evaluate the cooling performance of the CNT-based cooler, the average heat transfer coefficients were calculated for both the Cu-based cooler and the CNT-based cooler assuming the total surface area to be equal (Table 5). The average

heat transfer coefficients for the coolers under natural convection were about 36 $W \cdot m^{-2} \cdot K^{-1}$ and about 42 $W \cdot m^{-2} \cdot K^{-1}$ for Cu-cooler and CNT-cooler, respectively. Corresponding values under forced cooling (2.0 $L \cdot min^{-1}$) were about 140 $W \cdot m^{-2} \cdot K^{-1}$ and 150 $W \cdot m^{-2} \cdot K^{-1}$. The results show the potential of using MWCNTs as very effective heat dissipating material. The transferred CNT films were found to be useful in dissipating heat from ceramic chips with efficiency similar to that of integrated copper coolers.

**Table 5. The average heat transfer coefficients calculated for Cu-based and CNT-based coolers (Paper V, published by permission of Elsevier).**

| | h ($W \cdot m^{-2} \cdot K^{-1}$) | | | | |
|---|---|---|---|---|---|
| Gas flow ($L \cdot min^{-1}$) | 0.0 | 0.5 | 1.0 | 1.5 | 2.0 |
| Cu-based | 36 | 76 | 100 | 123 | 140 |
| CNT-based | 42 | 85 | 110 | 135 | 150 |

In summary, the solder transfer method is a fast, efficient and non-destructive transfer method for implementing CNT films in ceramic electronics which has potential for the large-scale production of large-area devices. Moreover, this type of non-destructive transfer on CNT films can be used in fabricating various other types of CNT-based devices, such as heat sinks.

# 6 Conclusions

The main objective in this thesis was to examine and demonstrate the integration of carbon nanotubes (CNTs) into existing manufacturing technologies used in the electronics industry. The CNTs were either chemically treated (for printed applications) or used as freestanding films (electrical contact brushes and thermal applications). The electrical, mechanical, and thermal properties of such carbon nanotubes based assemblies were characterized and furthermore demonstrated in various applications such as gas sensors, printed electronics, and electrical contact brushes and as a heat sink material in chip cooling applications.

Resistive gas sensors based on both SWCNT- and MWCNT-based inks were fabricated and their sensing performance towards nitric oxide ($NO_x$) was studied. SWCNT-based sensors showed superior performance compared to their MWCNT counterparts in all experiments, which could be explained by the larger, tuneable band gap of SWCNTs compared to that of MWCNTs.

The electrical transport mechanisms of inkjet-printed SWCNT films were studied and found to vary with their surface coverage. Dense CNT films displayed linear (ohmic behaviour), while low density networks had nonlinear (Schottky type) current–voltage characteristics suggesting that printed CNTs can be used as both interconnect and semiconducting films depending upon the thickness of the layers.

The feasibility of aligned multiwalled carbon nanotube brushes as a new high-performance electrical brush contact material was demonstrated. The MWCNT electrical contact brushes were used both as rotating axles and sliding contacts in electrical motors and exhibited stable, low-noise operation over long periods of operation.

The thermal properties (thermal diffusivity and conductivity) of individual carbon nanotubes in freestanding MWCNT forests were found to be comparable with those of conventional metals as measured by the flash method. The thermal conductivity of porous forests (~8 W/mK) suggests their application in thermal interfaces.

The good thermal properties as measured in aligned nanotube films were exploited in the cooling of ceramic ($Al_2O_3$) chips. The CNT structures were coated by a thin Cr/Au (15 nm/ 450 nm) solderable layer and subsequently soldered onto ceramic test chips using conventional SAC–paste (Sn–Ag–Cu). The cooling efficiency of such structures was found to be comparable to Cu-based reference coolers. The transfer process used is fast, efficient and non-destructing,

thus enabling large-scale manufacturing of CNT based assemblies in ceramic electronics and opening up possibilities for the large-scale production of large-area devices based on CNTs.

Most of the studies presented in the thesis are proof–of–concept demonstrations that highlight the possibilities of using carbon nanotubes as efficient replacement material in practical applications. The findings suggest that carbon nanotubes will be used in large-scale electrical assemblies in the future without requiring major modifications in the assembly methods already employed. The significant results obtained in this thesis emphasize not only the diverse and attractive properties of carbon nanotubes but also show the feasibility of utilizing their properties in various practical applications.

# References


Appenzeller J, Lin Y, Knoch J & Avouris P (2004) Band-to-band tunneling in carbon nanotube field-effect transistors. Physical Review Letters 93(19): 196805.

Avouris P (2002) Carbon nanotube electronics. Chemical Physics 281(2-3): 429-445.

Avouris P & Chen J (2006) Nanotube electronics and optoelectronics. Materials Today 9(10): 46-54.

Bachtold A, Strunk C, Salvetat J, Bonard J, Forro L, Nussbaumer T & Schönenberger C (1999) Aharonov-Bohm oscillations in carbon nanotubes. Nature 397(6721): 673-675.

Balasubramanian K & Burghard M (2005) Chemically functionalized carbon nanotubes. Small 1(2): 180-192.

Beecher P, Servati P, Rozhin A, Colli A, Scardaci V, Pisana S, Hasan T, Flewitt AJ, Robertson J, Hsieh GW, Li FM, Nathan A, Ferrari AC & Milne WI (2007) Ink-jet printing of carbon nanotube thin film transistors. Journal of Applied Physics 102(4): 043710.

Berber S, Kwon Y & Tománek D (2000) Unusually high thermal conductivity of carbon nanotubes. Physical Review Letters 2000(20): 4613-4616.

Borca-Tasciuc T, Vafaei S, Borca-Tasciuc D, Wei BQ, Vajtai R & Ajayan PM (2005) Anisotropic thermal diffusivity of aligned multiwall carbon nanotube arrays. Journal of Applied Physics 98(5): 054309-6.

Bruschi P, Cacialli F, Nannini A & Neri B (1994) Gas and vapor effects on the resistance fluctuation spectra of conducting polymer thin-film resistors. Sensors and Actuators B: Chemical 19(1-3): 421-425.

Cao A, Dickrell P, Sawyer W, Ghasemi-Nejhad M & Ajayan P (2005) Super-compressible foamlike carbon nanotube films. Science 310(5752): 1307-1310.

Cassell AM, McCool GC, Ng HT, Koehne JE, Chen B, Li J, Han J & Meyyappan M (2003) Carbon nanotube networks by chemical vapor deposition. Applied Physics Letters 82(5): 817-819.

Chen P, Fu Y, Aminirad R, Wang C, Zhang J, Wang K, Galatsis K & Zhou C (2011) Fully printed separated carbon nanotube thin film transistor circuits and its application in organic light emitting diode control. Nano Letters 11(12): 5301-5308.

Choi K & Yu C (2012) Highly doped carbon nanotubes with gold nanoparticles and their Influence on electrical conductivity and thermopower of nanocomposites. PLoS One 7(9): e44977.

Close GF, Yasuda S, Paul B, Fujita S & Wong H-P (2008) A 1 GHz integrated circuit with carbon nanotube interconnects and silicon transistors. Nano Letters 8(2): 706-709.

Collins P, Bradley K, Ishigami M & Zettl A (2000) Extreme oxygen sensitivity of electronic properties of carbon nanotubes. Science 287(5459): 1801-1804.

Datsyuk V, Kalyva M, Papagelis K, Parthenios J, Tasis D, Siokou A, Kallitsis I & Galiotis C (2008) Chemical oxidation of multiwalled carbon nanotubes. Carbon 46(6): 833-840.

Dettlaff-Weglikowska U, Skakalova V, Graupner R, Jhang S, Kim B, Lee H, Ley L, Park Y, Berber S, Tomanek D & Roth S (2005) Effect of SOCl2 treatment on electrical and mechanical properties of single-wall carbon nanotube networks. Journal of the American Chemical Society 127(14): 5125-5131.

Dresselhaus M, Dresselhaus G & Jorio A (2004) Unusual properties and structure of carbonnanotubes. Annual Review of Materials Research 34: 247-278.

Dresselhaus M, Dresselhaus G & Saito R (1992) Carbon-Fibers Based on C-60 and their Symmetry. Physical Review B 45(11): 6234-6242.

Dujardin E, Derycke V, Goffman M, Lefevre R & Bourgoin J (2005) Self-assembled switches based on electroactuated multiwalled nanotubes. Applied Physics Letters 87(19): 193107.

Ebbesen T, Lezec H, Hiura H, Bennett J, Ghaemi H & Thio T (1996) Electrical conductivity of individual carbon nanotubes. Nature 382(6586): 54-56.

Feng Y, Wang J, Zhang M & Xu Y (2007) The influence of pressure on the electrical tribology of carbon nanotube-silver-graphite composite. Journal of Materials Science 42(23): 9700-9706.

Fischer J, Dai H, Thess A, Lee R, Hanjani N, Dehaas D & Smalley R (1997) Metallic resistivity in crystalline ropes of single-wall carbon nanotubes. Physical Review B 55(8): R4921-R4924.

Fu Y, Nabiollah N, Wang T, Wang S, Hu Z, Carlberg B, Zhang Y, Wang X & Liu J (2012) A complete carbon-nanotube-based on-chip cooling solution with very high heat dissipation capacity. Nanotechnology 23(4): 045304.

Fu Y, Qin Y, Wang T, Chen S & Liu J (2010) Ultrafast transfer of metal-enhanced carbon nanotubes at low temperature for large-scale electronics assembly. Advanced Materials 22(44): 5039-5042.

Fuhrer M, Nygard J, Shih L, Forero M, Yoon Y, Mazzoni M, Choi H, Ihm J, Louie S, Zettl A & McEuen P (2000) Crossed nanotube junctions. Science 288(5465): 494-497.

Halonen N, Kordás K, Tóth G, Mustonen T, Mäklin J, Vähäkangas J, Ajayan PM & Vajtai R (2008) Controlled CCVD synthesis of robust multiwalled carbon nanotube films. Journal of Physical Chemistry C 112(17): 6723-6728.

Haspel H, Ionescu R, Heszler P, Kukovecz A, Konya Z, Gingl Z, Mäklin J, Mustonen T, Kordás K, Vajtai R & Ajayan PM (2008) Fluctuation enhanced gas sensing on functionalized carbon nanotube thin films. Physica Status Solidi B - Basic Solid State Physics 245(10): 2339-2342.

Holman JP (ed) (2002) Heat Transfer, 9th edition. New York, McGraw-Hill.

Hone J, Whitney M, Piskoti C & Zettl A (1999) Thermal conductivity of single-walled carbon nanotubes. Physical Review B 59(4): R2514-R2516.

Huang X, Wang J, Eres G & Wang X (2011) Thermophysical properties of multi-wall carbon nanotube bundles at elevated temperatures up to 830 K. Carbon 49(5): 1680-1691.

Iijima S (1991) Helical microtubules of graphitic carbon. Nature 354(6348): 56-58.

Ionescu MI, Zhang Y, Li R, Abou-Rachid H & Sun X (2012) Nitrogen-doping effects on the growth, structure and electrical performance of carbon nanotubes obtained by spray pyrolysis method. Applied Surface Science 258(10): 4563-4568.

Ivanov I, Puretzky A, Eres G, Wang H, Pan Z, Cui H, Jin R, Howe J & Geohegan DB (2006) Fast and highly anisotropic thermal transport through vertically aligned carbon nanotube arrays. Applied Physics Letters 89(22): 223110.

Jarillo-Herrero P, Sapmaz S, Dekker C, Kouwenhoven L & van der Zant H (2004) Electron-hole symmetry in a semiconducting carbon nanotube quantum dot. Nature 429(6990): 389-392.

Kaiser A, Dusberg G & Roth S (1998) Heterogeneous model for conduction in carbon nanotubes. Physical Review B 57(3): 1418-1421.

Kish L, Vajtai R & Granqvist C (2000) Extracting information from noise spectra of chemical sensors: single sensor electronic noses and tongues. Sensors and Actuators B: Chemical 71(1-2): 55-59.

Kleiner A & Eggert S (2001) Band gaps of primary metallic carbon nanotubes. Physical Review B 63(7): 073408.

Kong J, Franklin N, Zhou C, Chapline M, Peng S, Cho K & Dai H (2000) Nanotube molecular wires as chemical sensors. Science 287(5453): 622-625.

Kongkanand A, Dominguez RM & Kamat PV (2007) Single wall carbon nanotube scaffolds for photoelectrochemical solar cells: capture and transport of photogenerated electrons. Nano Letters 7(3): 676-680.

Kordás K, Tóth G, Moilanen P, Kumpumäki M, Vähäkangas J, Uusimäki A, Vajtai R & Ajayan PM (2007) Chip cooling with integrated carbon nanotube microfin architectures. Applied Physics Letters 90(12): 123105-3.

Kordás K, Mustonen T, Tóth G, Jantunen H, Lajunen M, Soldano C, Talapatra S, Kar S, Vajtai R & Ajayan PM (2006) Inkjet printing of electrically conductive patterns of carbon nanotubes. Small 2(8-9): 1021-1025.

Kuhlmann-Wilsdorf D (1996) Electrical fiber brushes-theory and observations. IEEE transactions on Components, Packaging, and Manufacturing Technology - Part A 19(3): 360-375.

Lee AP & Reedy BJ (1999) Temperature modulation in semiconductor gas sensing. Sensors and Actuators B: Chemical 60(1): 35-42.

Li J, Lu Y, Ye Q, Cinke M, Han J & Meyyappan M (2003) Carbon nanotube sensors for gas and organic vapor detection. Nano Letters 3(7): 929-933.

Li X, Ci L, Kar S, Soldano C, Kilpatrick SJ & Ajayan PM (2007) Densified aligned carbon nanotube films via vapor phase infiltration of carbon. Carbon 45(4): 847-851.

Liu J & Thomas P (2005) Exhaled breath condensate as a method of sampling airway nitric oxide and other markers of inflammation. Medical Science Monitor 11(8): MT53-MT62.

Long R & Yang R (2001) Carbon nanotubes as a superior sorbent for nitrogen oxides. Industrial & Engineering Chemistry Research 40(20): 4288-4291.

Lu Y, Partridge C, Meyyappan M & Li J (2006) A carbon nanotube sensor array for sensitive gas discrimination using principal component analysis. Journal of Electroanalytical Chemistry 593(1–2): 105-110.

Mäklin J, Mustonen T, Halonen N, Tóth G, Kordás K, Vähäkangas J, Moilanen H, Kukovecz Á, Kónya Z, Haspel H, Gingl Z, Heszler P, Vajtai R & Ajayan PM (2008) Inkjet printed resistive and chemical-FET carbon nanotube gas sensors. Physica Status Solidi B - Basic Solid State Physics 245(10): 2335-2338.

Mann D, Javey A, Kong J, Wang Q & Dai H (2003) Ballistic transport in metallic nanotubes with reliable Pd ohmic contacts. Nano Letters 3(11): 1541-1544.

McCurdy M, Bakhirkin Y, Wysocki G & Tittel F (2007) Performance of an exhaled nitric oxide and carbon dioxide sensor using quantum cascade laser-based integrated cavity output spectroscopy. Journal of Biomedical Optics 12(3): 034034.

Mehlich J, Miyata Y, Shinohara H & Ravoo BJ (2012) Fabrication of a carbon-nanotube-based field-effect transistor by microcontact printing. Small 8(14): 2258-2263.

Millward G & Jefferson D (1978) In: Walker Jr P & Thrower P (eds) Chemistry and physics of carbon. New York, Marcel Dekker: 1-82.

Mustonen T (2009) Inkjet printing of carbon nanotubes for electronic applications. Doctoral thesis. Oulu University Press, University of Oulu.

Naeemi A & Meindl JD (2007) Physical modeling of temperature coefficient of resistance for single- and multi-wall carbon nanotube interconnects. IEEE Electron Device Letters 28(2): 135-138.

Ni Y, Hung Le Khanh, Chalopin Y, Bai J, Lebarny P, Divay L & Volz S (2012) Highly efficient thermal glue for carbon nanotubes based on azide polymers. Applied Physics Letters 100(19): 193118.

Oberlin A, Endo M & Koyama T (1976) Filamentous Growth of Carbon through Benzene Decomposition. Journal of Crystal Growth 32(3): 335-349.

Park N & Hong S (2005) Electronic structure calculations of metal-nanotube contacts with or without oxygen adsorption. Physical Review B 72(4): 045408.

Parker WJ, Jenkins RJ, Butler CP & Abbott GL (1961) Flash method of determining thermal diffusivity, heat capacity, and thermal conductivity. Journal of Applied Physics 32(9): 1679-1684.

Penza M, Cassano G, Rossi R, Alvisi M, Rizzo A, Signore MA, Dikonimos T, Serra E & Giorgi R (2007) Enhancement of sensitivity in gas chemiresistors based on carbon nanotube surface functionalized with noble metal (Au, Pt) nanoclusters. Applied Physics Letters 90(17): 173123.

Pop E, Mann D, Wang Q, Goodson K & Dai H (2006) Thermal conductance of an individual single-wall carbon nanotube above room temperature. Nano Letters 6(1): 96-100.

Radushkevich L & Lukyanovich V (1952) About the structure of carbon formed by thermal decomposition of carbon monoxide on iron substrate. Zurn Fisic Chim 26: 88-95.

Sazonova V, Yaish Y, Ustunel H, Roundy D, Arias T & McEuen P (2004) A tunable carbon nanotube electromechanical oscillator. Nature 431(7006): 284-287.

Schönenberger C, Bachtold A, Strunk C, Salvetat J & Forro L (1999) Interference and Interaction in multi-wall carbon nanotubes. Applied Physics A-Materials Science & Processing 69(3): 283-295.

Shriver DF & Atkins PW (eds) (1999) Inorganic chemistry, 3rd edition. New York, Oxford University Press.

Skakalova V, Kaiser AB, Woo Y- & Roth S (2006) Electronic transport in carbon nanotubes: from individual nanotubes to thin and thick networks. Physical Review B 74(8): 085403.

Stadermann M, Papadakis S, Falvo M, Novak J, Snow E, Fu Q, Liu J, Fridman Y, Boland J, Superfine R & Washburn S (2004) Nanoscale study of conduction through carbon nanotube networks. Physical Review B 69(20): 201402.

Star A, Joshi V, Skarupo S, Thomas D & Gabriel JP (2006) Gas sensor array based on metal-decorated carbon nanotubes. Journal of Physical Chemistry B 110(42): 21014-21020.

Suehiro J, Imakiire H, Hidaka S, Ding W, Zhou G, Imasaka K & Hara M (2006) Schottky-type response of carbon nanotube NO2 gas sensor fabricated onto aluminum electrodes by dielectrophoresis. Sensors and Actuators B: Chemical 114(2): 943-949.

Sze SM (1981) Physics of semiconductor devices. In: Anonymous New York, Wiley-Interscience: 72.

Talapatra S, Kar S, Pal SK, Vajtai R, Ci L, Victor P, Shaijumon MM, Kaur S, Nalamasu O & Ajayan PM (2006) Direct growth of aligned carbon nanotubes on bulk metals. Nature Nanotechnology 1(2): 112-116.

Tawfick S, O'Brien K & Hart AJ (2009) Flexible high-conductivity carbon-nanotube interconnects made by rolling and printing. Small 5(21): 2467-2473.

Tóth G, Mäklin J, Halonen N, Palosaari J, Juuti J, Jantunen H, Kordás K, Sawyer WG, Vajtai R & Ajayan PM (2009) Carbon-nanotube-based electrical brush contacts. Advanced Materials 21(20): 2054-2058.

Troiani HE, Miki-Yoshida M, Camacho-Bragado G, Marques MAL, Rubio A, Ascencio JA & Jose-Yacaman M (2003) Direct observation of the mechanical properties of single-walled carbon nanotubes and their junctions at the atomic level. Nano Letters 3(6): 751-755.

Vaillancourt J, Zhang H, Vasinajindakaw P, Xia H, Lu X, Han X, Janzen DC, Shih W, Jones CS, Stroder M, Chen MY, Subbaraman H, Chen RT, Berger U & Renn M (2008) All ink-jet-printed carbon nanotube thin-film transistor on a polyimide substrate with an ultrahigh operating frequency of over 5 GHz. Applied Physics Letters 93(24): 243301.

Valentini L, Armentano I, Kenny JM, Cantalini C, Lozzi L & Santucci S (2003) Sensors for sub-ppm $NO_2$ gas detection based on carbon nanotube thin films. Applied Physics Letters 82(6): 961-963.

Varghese O, Kichambre P, Gong D, Ong K, Dickey E & Grimes C (2001) Gas sensing characteristics of multi-wall carbon nanotubes. Sensors and Actuators B: Chemical 81(1): 32-41.

Watts PCP, Mureau N, Tang Z, Miyajima Y, Carey JD & Silva SRP (2007) The importance of oxygen-containing defects on carbon nanotubes for the detection of polar and non-polar vapours through hydrogen bond formation. Nanotechnology 18(17): 175701.

Yamada T (2004) Modeling of carbon nanotube Schottky barrier modulation under oxidizing conditions. Physical Review B 69(12): 125408.

Yang M, Teo K, Milne W & Hasko D (2005) Carbon nanotube Schottky diode and directionally dependent field-effect transistor using asymmetrical contacts. Applied Physics Letters 87(25): 253116.

Yao Z, Postma H, Balents L & Dekker C (1999) Carbon nanotube intramolecular junctions. Nature 402(6759): 273-276.

Yorikawa H & Muramatsu S (1995) Energy gaps of semiconducting nanotubules. Physical Review B 52(4): 2723-2727.

Yu M, Lourie O, Dyer MJ, Moloni K, Kelly TF & Ruoff RS (2000) Strength and breaking mechanism of multiwalled carbon nanotubes under tensile load. Science 287(5453): 637-640.

Yun Y, Shanov V, Tu Y, Subramaniam S & Schulz MJ (2006) Growth mechanism of long aligned multiwall carbon nanotube arrays by water-assisted chemical vapor deposition. Journal of Physical Chemistry B 110(47): 23920-23925.

Zhang K, Chai Y, Yuen MMF, Xiao DGW & Chan PCH (2008) Carbon nanotube thermal interface material for high-brightness light-emitting-diode cooling. Nanotechnology 19(21): 215706.

Zhao J, Han J & Lu J (2002) Work functions of pristine and alkali-metal intercalated carbon nanotubes and bundles. Physical Review B 65(19): 193401.

Zhu H, Xu C, Wu D, Wei B, Vajtai R & Ajayan P (2002) Direct synthesis of long single-walled carbon nanotube strands. Science 296(5569): 884-886.

# Appendix 1

The electrical measurements of printed CNT networks (Paper II) were performed with Keithley Instruments dual-channel SourceMeters™ (models 2612 and 2636). For more convenient and practical measurements, custom control software was developed by the author using LabVIEW. The user gives the measurement parameters to the program and the program handles the measurement automatically and plots the measured curves on screen. Finally it saves the measurement results as a .txt file for further analysis.

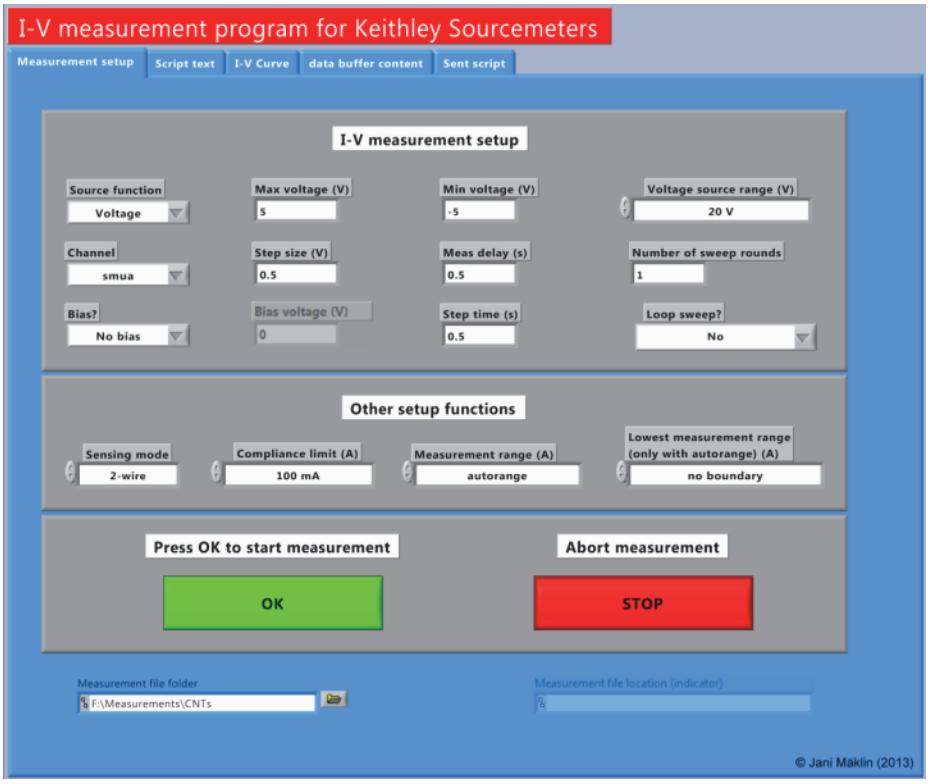


**Fig. 31. Front panel of the LabVIEW measurement program that was developed for characterizing printed nanotube films (Paper II). This window is displayed as the program is started. The user defines the measurement parameters and measurement starts after the OK button is pressed. The program can be used not only for measuring *I–Vs* ($I_{S\text{-}D}$ *vs.* $U_{S\text{-}D}$) measurements but also for gatesweep ($I_{S\text{-}D}$ *vs.* $U_G$) measurements.**

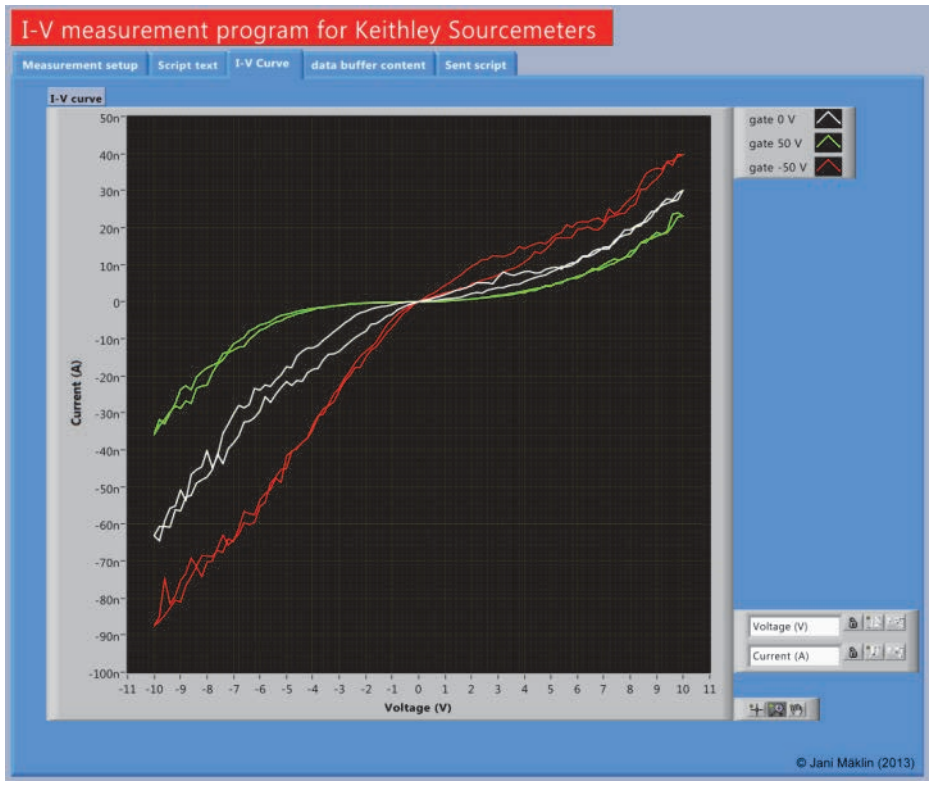


**Fig. 32. Front panel of the LabVIEW measurement program that was developed for characterizing printed nanotube films (Paper II). This window is displayed automatically as the measurement is finished.**

# Appendix 2

The DC electrical characterization in Paper III was performed with a combination of a Keithley Instruments AC and DC Current Source (model 6221) and a Nanovoltmeter (model 2182A). A custom LabVIEW program was developed by the author for controlling the devices in a semi-automated manner during the measurements. When the program is opened, the measurement setup window is displayed and the user can define the measurement parameters. After the measurement is finished, the measured *I–V* plot is shown and the measurement results are saved in a .txt file for further analysis.

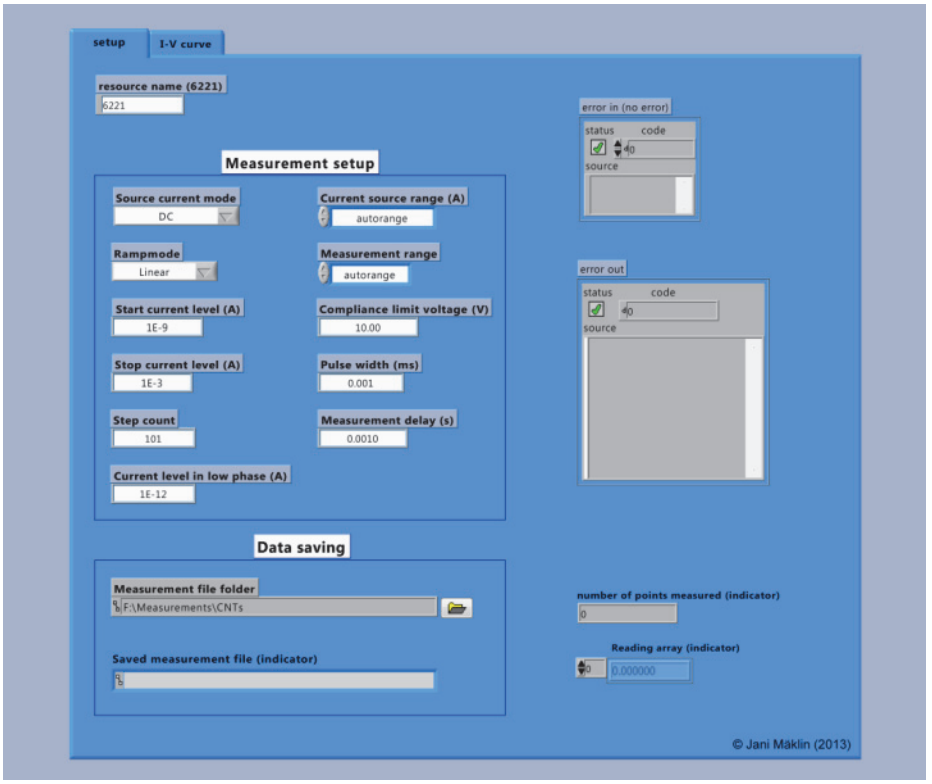


**Fig. 33. Front panel of the LabVIEW measurement program that was developed for characterizing robust nanotube films (Paper III). This window is displayed as the program is opened. The user defines the measurement parameters and the folder where the measurement file will be saved. The measurement starts after the program is launched by the user.**

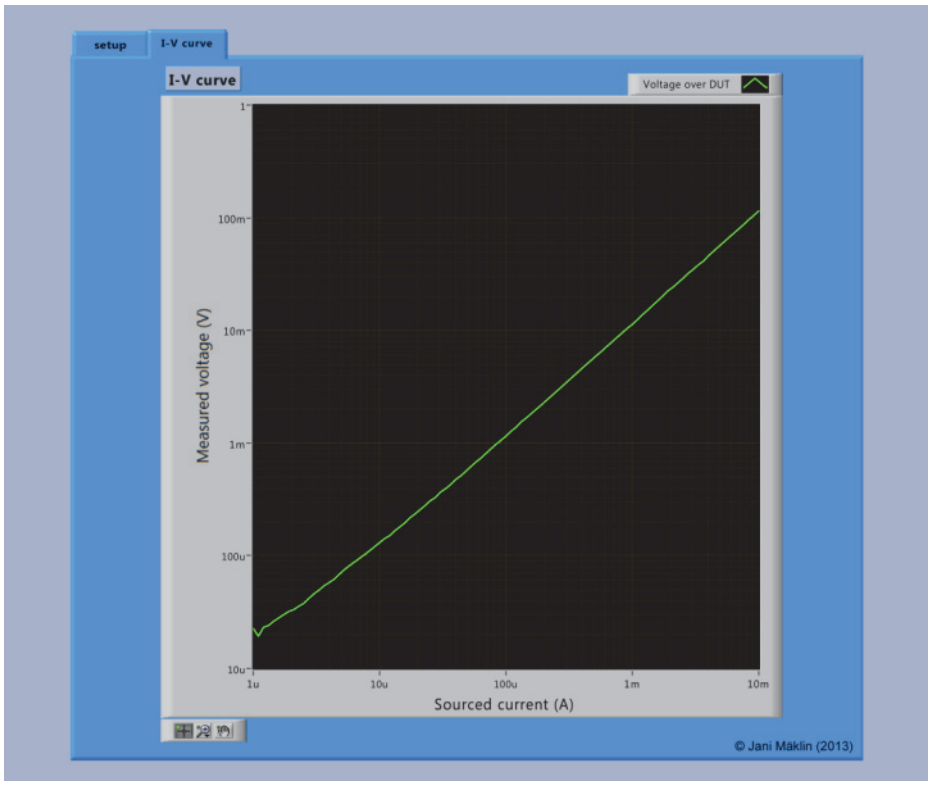


**Fig. 34. Front panel of the LabVIEW measurement program that was developed for characterizing robust nanotube films (Paper III). This window is displayed automatically as the measurement is finished.**

# Original publications

I Mäklin J, Mustonen T, Kordás K, Saukko S, Tóth G & Vähäkangas J (2007) Nitric oxide gas sensors with functionalized carbon nanotubes. Physica Status Solidi B 244(11): 4298–4302.

II Mustonen T, Mäklin J, Kordás K, Halonen N, Tóth G, Saukko S, Vähäkangas J, Jantunen H, Kar S, Ajayan PM, Vajtai R, Helistö P, Seppä H & Moilanen H (2008) Controlled Ohmic and nonlinear electrical transport in inkjet-printed single-wall carbon nanotube films. Physical Review B 77(12): 125430 1–7.

III Tóth G, Mäklin J, Halonen N, Palosaari J, Juuti J, Jantunen H, Kordás K, Sawyer WG, Vajtai R & Ajayan PM (2009) Carbon-Nanotube-Based Electrical Brush Contacts. Advanced Materials 21(1): 1–5.

IV Mäklin J, Halonen N, Tóth G, Sápi A, Kukovecz Á, Kónya Z, Jantunen H, Mikkola J-P & Kordás K (2011) Thermal diffusivity of aligned multi-walled carbon nanotubes measured by the flash method. Physica Status Solidi B 248(11): 2508–2511.

V Mäklin J, Halonen N, Pitkänen O, Tóth G & Kordás K (2014) Solder transfer of carbon nanotube microfin coolers to ceramic chips. Applied Thermal Engineering 65(1–2): 539–543.

Reprinted with permission from APS, Wiley-VCH and Elsevier.

Original publications are not included in the electronic version of the dissertation.

Book orders:
Granum: Virtual book store
http://granum.uta.fi/granum/

UNIVERSITY OF OULU P.O. Box 8000 FI-90014 UNIVERSITY OF OULU FINLAND

# ACTA UNIVERSITATIS OULUENSIS

SERIES EDITORS

A
**SCIENTIAE RERUM NATURALIUM**

*Professor Esa Hohtola*

B
**HUMANIORA**

*University Lecturer Santeri Palviainen*

C
**TECHNICA**

*Postdoctoral research fellow Sanna Taskila*

D
**MEDICA**

*Professor Olli Vuolteenaho*

E
**SCIENTIAE RERUM SOCIALIUM**

*University Lecturer Veli-Matti Ulvinen*

F
**SCRIPTA ACADEMICA**

*Director Sinikka Eskelinen*

G
**OECONOMICA**

*Professor Jari Juga*

EDITOR IN CHIEF

*Professor Olli Vuolteenaho*

PUBLICATIONS EDITOR

*Publications Editor Kirsti Nurkkala*

ISBN 978-952-62-0385-0 (Paperback)
ISBN 978-952-62-0386-7 (PDF)
ISSN 0355-3213 (Print)
ISSN 1796-2226 (Online)

UNIVERSITY of OULU
OULUN YLIOPISTO